

# Explaining sudden losses of outer radiation belt electrons during geomagnetic storms

Drew L. Turner, Yuri Shprits, Michael Hartinger, and Vassilis Angelopoulos

Correspondence to: [drew.lawson.turner@gmail.com](mailto:drew.lawson.turner@gmail.com)

## **This file includes:**

Materials and Methods  
Additional Study Details  
Additional References  
Figs. S1 to S14

## Materials and Methods

### Solar Wind and Geomagnetic Indices

The OMNI dataset, available online at: <http://omniweb.gsfc.nasa.gov/>, consists of solar wind data propagated to Earth's subsolar bow shock. Here we use OMNI data at 1-minute resolution. Solar wind plasma and magnetic field data from the ACE spacecraft in orbit around the first Sun-Earth Lagrange point are shown in Figure S7. This confirms the OMNI data shown in Figure 1, and it also shows the calm conditions before the CIR and storm on the 6th.

Also used for this study are the Dst and Kp geomagnetic indices. These are available from the Kyoto World Data Center for Geomagnetism (see website at: <http://wdc.kugi.kyoto-u.ac.jp/wdc/Sec3.html>). The Dst index is widely used to determine timing and intensity of geomagnetic storms, as it is a good indicator of ring current activity. The Kp index represents more general geomagnetic activity, and it is used as the independent variable in many empirical models. For example, Kp is used to determine the approximate plasmopause locations shown in Figure 2. These indices are also inputs to the Tsyganenko-2001 Storm and -1989 models used for this study.

### GOES-13 EPEAD Dataset

The GOES-13 spacecraft at geosynchronous orbit measures electrons in three integral flux channels, >800 keV, >2 MeV, and >4 MeV, using the Energetic Proton, Electron, and Alpha particle Detector (EPEAD). For details on this instrument, see: <http://www.swpc.noaa.gov/Data/goes.html>. These data are freely available at the NOAA-NGDC website: <http://www.ngdc.noaa.gov/stp/>. For this study, we only use the >800 keV channel, since the other two are at background flux levels during the flux dropout event (e.g. see Figure S1). Five-minute resolution data are used.

### GOES MAGED Dataset

The latest generation of GOES spacecraft, starting with GOES-13, carry additional energetic particle instrumentation. Here, we employ the Magnetospheric Electron Detector (MAGED) instrument from GOES-13 and -15. Like the EPEAD data, these data are freely available at the NOAA-NGDC website. The instrument package for electrons consists of 9 telescopes mounted onto the spacecraft at different angles, which provide pitch angle information. The field of view of these telescopes is 30 degrees. The instruments each measure differential flux in five energy channels: 30-50 keV, 50-100 keV, 100-200 keV, 200-350 keV, and 350-600 keV. Proton contamination in the electron fluxes is removed using the 80-800 keV proton measurements from the MAGED counterparts for protons, the Magnetospheric Proton Detectors (MAGPD), which are also on the latest generation GOES spacecraft. Here, we use 1-minute resolution MAGED data, and pitch angles for each instrument have been calculated using their respective orientation on each spacecraft and the local magnetic field, which is measured directly by magnetometers on each GOES spacecraft.

### NOAA-POES Dataset

Since 1998, an upgraded version of the Space Environment Monitor (SEM-2) on the NOAA-POES satellites in Sun-synchronous, low-Earth orbits (altitude ~850 km) has provided measurements of energetic protons and electrons over a very broad range of L-shells. As part of SEM-2, the Medium Energy Proton and Electron Detector (MEPED) monitors electrons in three integral channels, >30 keV, >100 keV, and >300 keV within a 30 degree field of view. On each POES spacecraft, two MEPED instruments are mounted orthogonal to each other such that particles with local pitch angles of around 0 and 90 degrees can be measured simultaneously. Evans and Greer [2004] provide a detailed description of SEM-2, and they also discuss how protons between 210 and 2700 keV can contaminate the MEPED electron channels. Fortunately, however, MEPED also measures protons in this energy range, and methods have been developed to decontaminate the electron data.

Here, we use 16-second resolution MEPED data from six of the POES spacecraft: NOAA-15, -16, -17, -18, and -19 and the METOP-02 spacecraft. The data from the 0 degree instrument are interpreted as representing the precipitating population in the loss cone. Those from the 90-degree instrument are interpreted as trapped, which is well-established for outer belt L-shells based on previous studies using

these data [e.g. Horne et al., 2009; Sandanger et al., 2009; Lam et al., 2010; Rodger et al, 2010]. To correct for the proton contamination in the electron data, we employ the technique used by Horne et al [2009] and Lam et al. [2010]. This correction involves determining an appropriate proton energy spectrum based on the proton data and integrating it over the known contamination energy ranges for each electron channel to subtract that from the electron counts. Simulations and tests have shown that the >30 keV, >100 keV, and >300 keV electron channels are sensitive to 210-2700 keV, 280-2700 keV, and 440-2700 keV protons respectively. Four MEPED proton channels, 80-240 keV, 240-800 keV, 800-2500 keV, and 2500-6900 keV, cover this energy range, and each is considered free of external contamination. These channels are fit with an energy spectrum assuming that the spectrum in each channel can be approximated as an exponential. Thus, the total energy spectrum over the full range is a piecewise function of exponentials representing the spectra from each proton channel. Initial guesses for the spectral fitting parameters are determined, and the “bowtie” method described in Selesnick and Blake [2000] is then used in an iterative scheme to settle upon the final parameters used to make the correction. For detailed descriptions of this method applied to POES data, see Appendix A of Lam et al. [2010].

### THEMIS Dataset

NASA’s Time History of Events and Macroscale Interactions during Substorms (THEMIS) mission currently consists of three (five originally), identically instrumented spacecraft in highly eccentric orbits near the magnetic equatorial plane [Angelopoulos, 2008]. THEMIS also incorporates an extensive network of ground magnetometers throughout Canada and Alaska. For this study, we use THEMIS-Solid State Telescope (SST) energetic electron data and magnetometer data from the three probes as well as the McGrath ground station in Alaska ( $L \sim 5 R_E$ ). In early January 2011, THEMIS-A (TH-A), -D, and -E reached their apogees on Earth’s late-morning dayside at around 08:00 local time. Thus, as the probes traversed the outer radiation belt, their outbound passes were in the early-morning local time sector around dawn, and their inbound passes were in the late-morning/pre-noon local time sector.

The most readily available SST data consist only of those derived from just one of the three available detectors in each instrument [e.g. Ni et al., 2011]. They constitute the first 12 energy channels for electrons and ions. However, four additional energy channels for both ion and electrons use coincident logic for various combinations of the three available detectors in each SST. The first 12 SST channels are known to suffer from contamination effects while THEMIS is in radiation belts, but the coincidence logic applied for the remaining channels effectively removes this contamination, as shown in Figure S8. From Figure 8, note how using the coincidence logic effectively removes the proton contamination from the electron data, revealing the well-known slot and inner belt regions that are not apparent in the data from the first 12 channels only. Based on ongoing calibrations of the SST instrument, the three foil-thick channels measure electrons with energy ranging from 300 keV – 750 keV. For our qualitative comparison shown in Figure 2 of the paper and Figure S2 here, we use the first coincidence channel only, which corresponds to approximately 400 keV electrons.

We obtained magnetic field data from the THEMIS McGrath (MCGR) ground magnetometer at 2 Hz sampling rate. MCGR is located at 63.0 degrees geographic latitude and 204.4 degrees geographic longitude, corresponding to  $L$  of  $\sim 5 R_E$ . The magnetic field data are in HDZ coordinates, where H points to the north magnetic pole, Z is vertically downward, and D completes the set (roughly eastward). We computed the DC field of the D component by applying a low-pass filter (frequency  $< 0.5$  mHz). This DC field was then subtracted from the D component to obtain the AC field (frequency  $> 0.5$  mHz) shown in Figure 1e. To better characterize the global extent and time evolution of the ULF wave activity, we supplemented the MCGR data with 3 other stations at comparable geomagnetic latitude (S18). These include the THEMIS magnetometers White Horse (WHIT) and Goose Bay (GBAY), the CARISMA magnetometer Gillam (GILL), and the IMAGE magnetometer Dønna (DON).

We obtained fluxgate magnetometer data from the THEMIS-A (THA) probe at 0.33 Hz sampling rate. We computed the DC total magnetic field by low pass filtering (frequency  $< 0.5$  mHz). This DC field was then subtracted from the total magnetic field to obtain the AC total magnetic field (frequency  $> 0.5$  mHz). Finally, we applied a running fast Fourier transform (FFT) to the AC total magnetic field for two intervals, one before and one after the pressure pulse, shown in Figure 1, panels f and g. The FFT window size was about 50 minutes to accommodate waves with frequencies above 1 mHz.

## Additional Study Details

### Proof that the Dropout is Non-Adiabatic

It is critical to the results presented here that the dropout can be shown to be non-adiabatic, i.e., in violation of one or more of electrons' three adiabatic invariants. Energetic particles trapped in Earth's magnetic field undergo three characteristic motions: gyration around field lines, bounce along field lines between mirror points, and drift around the entire system. The gyro-motion is the fastest of these three motions, whereas drift is the slowest; a ~1 MeV electron at GEO with an equatorial pitch angle of 60 degrees has a gyro-period of  $\sim 10^{-3}$  s, a bounce-period of  $\sim 1$  s, and a drift period of  $10^3$  s. Associated with each of these motions is an adiabatic invariant, which is conserved so long as the field is not changing with frequencies comparable to the associated motion's frequency or on spatial scales comparable to that of the motion. These invariants are useful for radiation belt studies since PSD can be defined in a 3-dimensional invariant space using them, and according to Liouville's theorem, PSD for fixed invariants is conserved along a particle's trajectory in phase space in the absence of additional source or loss processes.

The three adiabatic invariants associated with trapped energetic particle motion in Earth's magnetic field are:

$$\mu = \frac{p_{\perp}^2}{2m_0B} \quad (1)$$

$$J = \oint p_{\parallel} ds; \quad K = \frac{J}{2\sqrt{2m_0\mu}} \quad (2)$$

$$\Phi = \oint \vec{B} \cdot d\vec{A}; \quad L^* = \frac{2\pi M}{\Phi R_E} \quad (3)$$

where  $\mu$ ,  $J$ , and  $\Phi$  are the first, second, and third invariants associated with gyro-, bounce, and drift motion respectively.  $p$  is relativistic momentum,  $m_0$  is the electron rest mass,  $B$  is local magnetic field strength,  $A$  is the area enclosed by a drift shell at the magnetic equator, and  $M$  is Earth's magnetic moment. Thus, the first invariant is proportional to an electron's perpendicular momentum (and thus its energy) and inversely to the local magnetic field strength. The second invariant is the integral of an electron's parallel momentum along one full bounce between magnetic mirror points.  $K$  is also shown; it is another invariant term that is used more than  $J$ , as it is decoupled from the first invariant. The third invariant is essentially the amount of magnetic flux enclosed by an electron's drift shell.  $L^*$ , which defines the electron's invariant drift shell, is in units of  $R_E$ .

Flux dropouts in the main phase of geomagnetic storms were originally thought to be simply a result of adiabatic transport of outer belt electrons. In the main phase when Earth's magnetic field is significantly reduced by an enhanced ring current, electrons' drift shells will expand to conserve the third adiabatic invariant. Although  $L^*$  will stay the same, the drift shell will expand in physical space. Additionally, as the drift shells expand and electrons move to regions of weaker magnetic field further from the Earth, they will lose energy to conserve their first adiabatic invariant. Thus, a spacecraft measuring electron flux (which can be used to calculate PSD, see Eq. 4 below) at one location during this change will observe electrons before the storm at energy lower than that during the main phase. Since electron fluxes in the outer belt decrease exponentially with increasing energy, it was thought that this could fully explain the flux dropout. After the field returns to its pre-storm levels, the electrons should move back in while conserving their invariants, and this should return the flux level to its pre-storm state. In other words, adiabatic variations are reversible and cannot produce a net change in fluxes after the magnetic field recovers to pre-storm conditions. Any irreversible variations must result from source or loss active during the storm's main and recovery phases. However, many recent studies (see citations from paper) show that dropouts are non-adiabatic.

We use GOES-13 >800 keV fluxes during the storm on 06 Jan. 2011 to demonstrate that the main phase dropout associated with this storm is non-adiabatic. Figure S1 shows GOES-13 fluxes from the >800 keV and >2 MeV channels. Also shown are magnetic fields measured by GOES-13 (blue) and modeled (green) for the spacecraft location using the Tsyganenko-2001 Storm model [Tsyganenko et al., 2003] and the  $L^*$  for GOES-13 calculated using the same model. Data values are provided for two times, one before ( $t = 0.351 = 08:24$  UT on 6 Jan) and one during ( $t = 1.035 = 00:50$  UT on 7 Jan) the storm. At these times, GOES-13 is on the same drift shell, i.e.  $L^* \sim 6.36 R_E$ . Additionally, the field strength measured by GOES-13 is approximately the same, around 88 nT +/- 2 nT, which means that the first adiabatic invariant calculated for ~800 keV electrons at these two times would be approximately the same (see Eq. 1). Finally, we assume that the majority of electrons measured are peaked at ~90 degrees, which is an approximation used to derive PSD gradients in a previous study using GOES electron measurements [i.e. Onsager et al., 2004]. This implies that the three adiabatic invariants at these two times would be the same for these GOES-13 measurements. However, the flux at these times differs by two orders of magnitude. Recall that flux is used to calculate the PSD using:

$$f = \frac{J}{p^2} \quad (4)$$

where  $f$  is PSD and  $j$  is flux. So the PSD for fixed invariants at these two times would also differ by a factor on the order of  $10^2$ . This is evidence that the main phase dropout was non-adiabatic, at least near GEO.

There is more evidence to support that the dropout was non-adiabatic as well. First, from the GOES-MAGED data, it is possible to directly calculate the PSD and first adiabatic invariants for electrons with pitch angles of ~90 degrees at each GOES spacecraft. Figures S15 and S16 show these parameters calculated for GOES-13 for 00:00 UT on 06 Jan. to 06:00 UT on 07 Jan. As in Figure S1, data points have been marked for the times when all three invariants are the same during the quiet time before and just after the flux dropout. Here, the equivalent energy used to calculate PSD and  $\mu$  is calculated for each energy channel as the square root of the product of the channel's maximum and minimum energies, following Chen et al. [2007]. Thus, for the times marked on each plot, it is evident that the PSD for  $\mu = 497$  MeV/G electrons, corresponding to the fluxes at GOES between 350 and 600 keV, has dropped by two orders of magnitude even though the first, second, and third invariants are the same. When comparing the  $L^*$ s calculated using different models at these times, error can be estimated. We compared  $L^*$ s calculated using the Tsyganenko-1989, 2001-storm, and 2005 models [Tsyganenko et al., 1989; 2003; 2005]. The difference in  $L^*$  at the chosen time before the storm was less than  $0.2 R_E$ . For the chosen time during the storm main phase, the maximum difference was  $\sim 0.8 R_E$ , and based on previous studies of PSD radial gradients [Fennell and Roeder, 2008; Turner et al., 2010], the PSD for fixed first and second invariants varies by less than one order of magnitude within  $1 R_E$  of GEO during quiet conditions. Thus, error in the  $L^*$  calculation based on the field model is not enough to account for the drop in PSD observed during the storm. This validates the first argument presented above (using the GOES EPEAD and magnetometer data) that this dropout included non-adiabatic losses. It is also of interest to note that the PSD difference at these times is much less for the lower-energy electrons, which is further evidence that the low-energy population of electrons was repopulated by a source in the plasma sheet during the main phase of the storm.

Figure S9 shows NOAA-POES >300 keV electron fluxes similar to Figure 1 from the paper. However, in Figure S9, the fluxes have been binned by  $L^*$  calculated using the Tsyganenko 2001-storm model. For fixed  $L^*$ s, the dropout also occurs. Finally, Figure S10 shows POES proton data from three different energy channels. The higher-energy protons in the bottom two plots exhibit substorm injections during the main phase of the storm, which means they have a significant source in the plasma sheet. The 30-80 keV electrons, however, experience a main phase dropout like that of the outer belt electrons. Interestingly, the length of the dropout for the protons is significantly longer than that for the >300 keV electrons, which would not be expected were the variation a result of adiabatic motion. The proton dropout at  $L$  between 5 and  $6 R_E$  persists for approximately one full day, while that of the electrons lasts only around 8 hours. Since both populations are stably trapped at these radial distances, a fully adiabatic response to the storm's main phase should result in the same flux dropout and return times for all trapped

particles. Interestingly, these protons should be subject to the same loss mechanism as the electrons, i.e., via magnetopause shadowing followed by enhanced outward radial transport. The difference in their respective recoveries can then be explained by different source mechanisms operating during the recovery phase.

### ULF Wave Analysis

Following Brautigam and Albert [2000] and Loto'aniu et al. [2010], we have calculated the electric and magnetic field components of the diffusion coefficients using fields observed during the main phase of this storm. Figure S18 shows a map of ground magnetometer stations used to calculate the magnetic  $D_{LL}$ s and the measured field components with and without the background field removed during the main phase of the storm. This figure tells us that the ULF activity during this period is global, since stations over this broad local time range all observe enhanced ULF wave activity. This is also apparent in the power spectral density plots shown in Figure S19. From these power spectral densities, the diffusion coefficients can be calculated using:

$$D_{LL}^E = \frac{1}{8B_s^2 R_E^2} \cdot L^6 \cdot \sum_{m=1} P_m^E \quad (5)$$

$$D_{LL}^B = \frac{\mu^2}{8q^2 \gamma^2 B_s^2 R_E^4} \cdot L^4 \cdot \sum_{m=1} m^2 P_m^B \quad (6)$$

following Falthammar [1965].

In these calculations, we made the following assumptions. First, we used mode number,  $m = 1$ , since the wave activity is global and driven predominantly by the solar wind. This assumption does not affect the calculations unless the  $m$  number is significantly increased, which would be inconsistent with the solar wind driver. We calculated the wave power spectral densities at  $L = 5$  and map the diffusion coefficient to other  $L$ -shells using the storm-time  $D_{LL}$   $L$ -dependence from Selesnick and Blake [2000]. We approximated the field strength as that for a dipole, and to account for some cold plasma contamination in the THEMIS-A electric field measurements, we estimated fluctuations in the electric field as being on the order of 1-2 mV/m. Figure S20 shows the resulting  $D_{LL}$  for  $\mu = 2000$  MeV/G electrons with the Brautigam and Albert [2000] and Selesnick and Blake [2000]  $D_{LL}$ s also shown for comparison. This shows that the diffusion coefficient based on the wave activity observed during this storm's main phase is enhanced in comparison to standard models.

### Modeling: Proof of Concept

To test this scenario, we use a very simple, one-dimensional radial diffusion model of the form:

$$\frac{\partial f}{\partial t} = L^{*2} \frac{\partial}{\partial L^*} \left( \frac{D_{LL}}{L^{*2}} \frac{\partial f}{\partial L^*} \right) \quad (7)$$

where  $D_{LL}$  is the diffusion coefficient, which along with the radial gradient specifies the rate of radial diffusion. The results of several model runs are shown in Figure S3. For these runs, we use two well-accepted forms of  $D_{LL}$ , namely those of Brautigam and Albert [2000] and Selesnick and Blake [2000]. For the Brautigam and Albert [2000] coefficient, which is dependent on the  $K_p$  index, we use  $K_p = 5.0$ , which is the  $K_p$  during the main phase dropout on 06 Jan. 2011. In Figure S3 a) and b), the model is simply allowed to run based on the initial condition shown (darkest blue is initial time). The initial distribution is selected to be very gently peaked, leaving it essentially flat beyond GEO. This is consistent with the results of Turner et al. [2010], which showed that PSD radial gradients for relativistic electrons beyond GEO are often flat during several day periods of calm solar wind and geomagnetic conditions, as was the case prior to this storm.

Figure S3 c) and d) start with the same distribution, but at the 10<sup>th</sup> time step, the PSD at  $L^* \geq 7.5 R_E$  are reduced to 1 percent of the initial distribution maximum. This effectively simulates the loss at higher  $L$ -shells due to the magnetopause moving inward in response to the enhanced solar wind dynamic pressure. After this time step, the outer boundary is held at this value, and the system continues to diffuse. The sharp

gradient that remains after the loss at higher L-shells results in very rapid outward diffusion, which drastically drops the PSD at higher L-shells. Note that above  $L^* \sim 4.5 R_E$ , both the Selesnick and Blake [2000] and the Brautigam and Albert [2000] results show very significant drops in PSD, which will be reflected in electron fluxes. Also, since the diffusion at these higher L-shells is outward and the electrons conserve their first adiabatic invariant, they become less energetic as they are transported outward in the system. Thus, the flux dropout for any given energy will be even more enhanced than by the drop in PSD alone. Finally, note the time scale that both models reveal for the dropout: it occurs over a broad range of L-shells in less than 3 hours. When the higher diffusion coefficients calculated from the ULF observations during this event are used (see above), the dropout also occurs in less than 3 hours and extends to below  $L^* = 4$ .

These results are consistent with the more detailed modeling conducted by Brautigam and Albert [2000], Miyoshi et al. [2003] and Shprits et al. [2006], who used radial diffusion codes and  $L^*$ -derived boundary conditions. In that work as well as the work shown here, the outer boundary condition is of course a very important factor in the model results. In reality, the PSD beyond the last closed drift shell is much lower than that in the stably trapped region, which might lead one to ask why this rapid diffusion doesn't occur all the time. In reality, several factors likely play a role. First, outward diffusion should always be occurring at this outer boundary, resulting in loss to the system. However, the outer boundary is not a rigid one; there is a finite, quasi-trapped region of partial drift shells, in which electrons can drift around most of the system up to some point on the dawn-side of the subsolar point. The quasi-trapped region will serve as a buffer under normal conditions but will be fully depleted along with the previously closed drift shells at higher  $L^*$  when the magnetopause is moved rapidly inwards in response to enhanced solar wind dynamic pressure. Also, under normal conditions, there is an ongoing internal source of relativistic electron PSD that we have not included in these models. Essentially, in addition to the persistent loss along the pre-noon magnetopause from electrons diffusing into the buffer region, there is continual source from either the nightside via convection (primarily for the lower energy electrons) or outward diffusion from a local source within the belt (primarily for the relativistic electrons). In a steady-state condition, the sources will balance with any ongoing loss and outward diffusion through the buffer region to produce a distribution that is relatively flat between the peak in PSD (i.e. the heating zone, assuming internal source) and the outer boundary. The simple model shown here simply assumes that steady state as an initial condition. This steady state picture is consistent with the results of Turner et al. [2010], who observed PSD gradients resulting from various solar wind preconditioning, as previously mentioned. Further factoring into this picture is the ULF wave activity, which ultimately breaks the third adiabatic invariant allowing for diffusion to occur. Since electrons undergoing outward radial diffusion move into a region of weaker magnetic field, conservation of the 1<sup>st</sup> and 2<sup>nd</sup> invariants results in additional non-adiabatic loss of energy. Under the normal conditions prior to the storm, the ULF activity at L-shells throughout the belt is significantly weak, as shown in Figure 1. However, the ULF activity becomes enhanced during the main phase, allowing for the rapid diffusion to occur down to low L-shells (at least  $L \sim 4 R_E$ ). The model results shown here are a very simple proof of concept showing that based on our current understanding of diffusion rates and PSD distributions, we can reproduce flux dropouts throughout most of the outer belt in the same amount of time as is observed in situ.

To provide some additional evidence in support of this theory, Figure S17 shows GOES-13 and GOES-15 MAGED pitch angle distributions. This is a very complex series of plots. Considering that the spacecraft are separated in local time around GEO, with GOES-15  $\sim 1$  hour behind GOES-13 and that the spacecraft are moving tailward (i.e. on the dusk side of their orbits), GOES-13 is continually at higher  $L^*$  than GOES-15. The first drop in fluxes at all energies (shown in color) and pitch angles between 21:00 and 21:50 is due to the adiabatic response from the solar wind dynamic pressure dropping during this period. However, starting at around 22:30, GOES-13 observes a drop in fluxes first at 90 degrees and then at lower and higher pitch angles at later times. Interestingly, shortly after this, GOES-15 observes the same thing. Taking drift shell splitting into account (and using the  $L^*$ s for each spacecraft provided below each of the plots), what is observed is a drop in fluxes starting first at higher  $L^*$  and then propagating to lower  $L^*$ . This is consistent with what we would expect to see from enhanced outward radial transport in response to a sharp gradient left over from magnetopause shadowing.

### Additional Analysis with NOAA-POES Dataset

To ensure our understanding and interpretation of the NOAA-POES data, we have performed additional analysis with the dataset. Figure S11 shows the full dataset compiled from the 6 available spacecraft in the same format as Figure 2 from the paper but binned at a much higher time resolution (1-min). Focusing on the dropout, it is clear from these data that there are no localized precipitation events during the dropout, which confirms our conclusion based on the 30 minute binned data that there is insufficient loss to the atmosphere to explain the dropout. Figure S12 shows the NOAA-POES data separated by northern and southern hemispheres, which clearly exhibits the effects of the South Atlantic Anomaly (SAA). The enhanced flux bands in the slot region below  $L \sim 4.5 R_E$  are from individual spacecraft measuring enhanced fluxes as they pass through the SAA region. In the SAA region, spacecraft sample more intense fluxes of electrons with higher equatorial pitch angles than those at the same altitude outside the SAA. Note, however, that the flux enhancement at  $L \sim 4 R_E$  is present in both hemispheres, which indicates that it is independent of the SAA. Figure S13 separates the data by MLT sectors (dawn, noon, dusk, and midnight quadrants in magnetic local time). These more clearly deconvolute the SAA in the data, revealing enhanced fluxes in the slot region at different UTs for each MLT sector and a 24-hour cadence. This reflects Earth's rotation under the spacecraft. Note once again, that the enhanced flux near  $4 R_E$  at  $\sim 00:00$  UT on 07 Jan. appears at the same time in different MLT sectors, further confirming that it is not associated with the SAA. This flux enhancement is interesting, though since it does not directly pertain to the conclusions of this work, further interpretation of it will be left to ongoing study of this event.

With the NOAA-POES dataset, it is also possible to observe the  $>1$  MeV electron fluxes through the outer radiation belt [e.g. Horne et al., 2009; Sandanger et al., 2009]. These measurements are indirect as they actually rely on the  $>6.9$  MeV proton channel, which is also sensitive to  $>1$  MeV electrons, and through the outer belt when there have been no recent solar energetic particle events, the electron signal at these energies far outnumber that from such high-energy protons. Figure S14 shows this  $>1$  MeV electron data in the same format as Figure 2a. This reveals that there was a weak population of  $>1$  MeV electrons prior to the dropout. These electrons experience the same dropout as the lower energy electrons observed by GOES, THEMIS, and NOAA-POES. Consistent with the  $>300$  keV data, these electrons reveal no enhanced precipitation to the atmosphere throughout any part of the belt, which is further evidence that the non-adiabatic losses must be due to magnetopause shadowing resulting in enhanced outward radial diffusion. After  $\sim 1$  day, this  $>1$  MeV population returns and becomes enhanced during the recovery phase of the storm.

### Results from Other Storms

As mentioned in the paper, we have checked the results for three other storms, namely some of those studied in Onsager et al. [2002], Green et al. [2004], and Loto'aniu et al. [2010]. The NOAA-POES data from these storms are shown in the same format as Figure 2a in Figures S4 - S6. The Loto'aniu et al. [2010] and Onsager et al. [2002] storms were clearly shown to involve non-adiabatic losses, and Loto'aniu et al. [2010] also concluded that these were likely the result of magnetopause shadowing resulting in outward radial diffusion. However, they showed no evidence that there was not loss to the atmosphere. The NOAA-POES data shown here confirms that there is insufficient loss to the atmosphere to account for the non-adiabatic loss during these storms. In all three storms, some enhanced loss to the atmosphere is apparent at lower L-shells, around where the plasmapause is located below  $L \sim 5 R_E$ . This signifies that scattering due to wave particle interactions may play some role at these low L-shells, which agrees with Bortnik et al. [2006], however, the precipitating fluxes cannot fully account for the flux dropout throughout the entire belt. This reveals that magnetopause shadowing resulting in enhanced outward radial diffusion well explains the observations during these events as well.

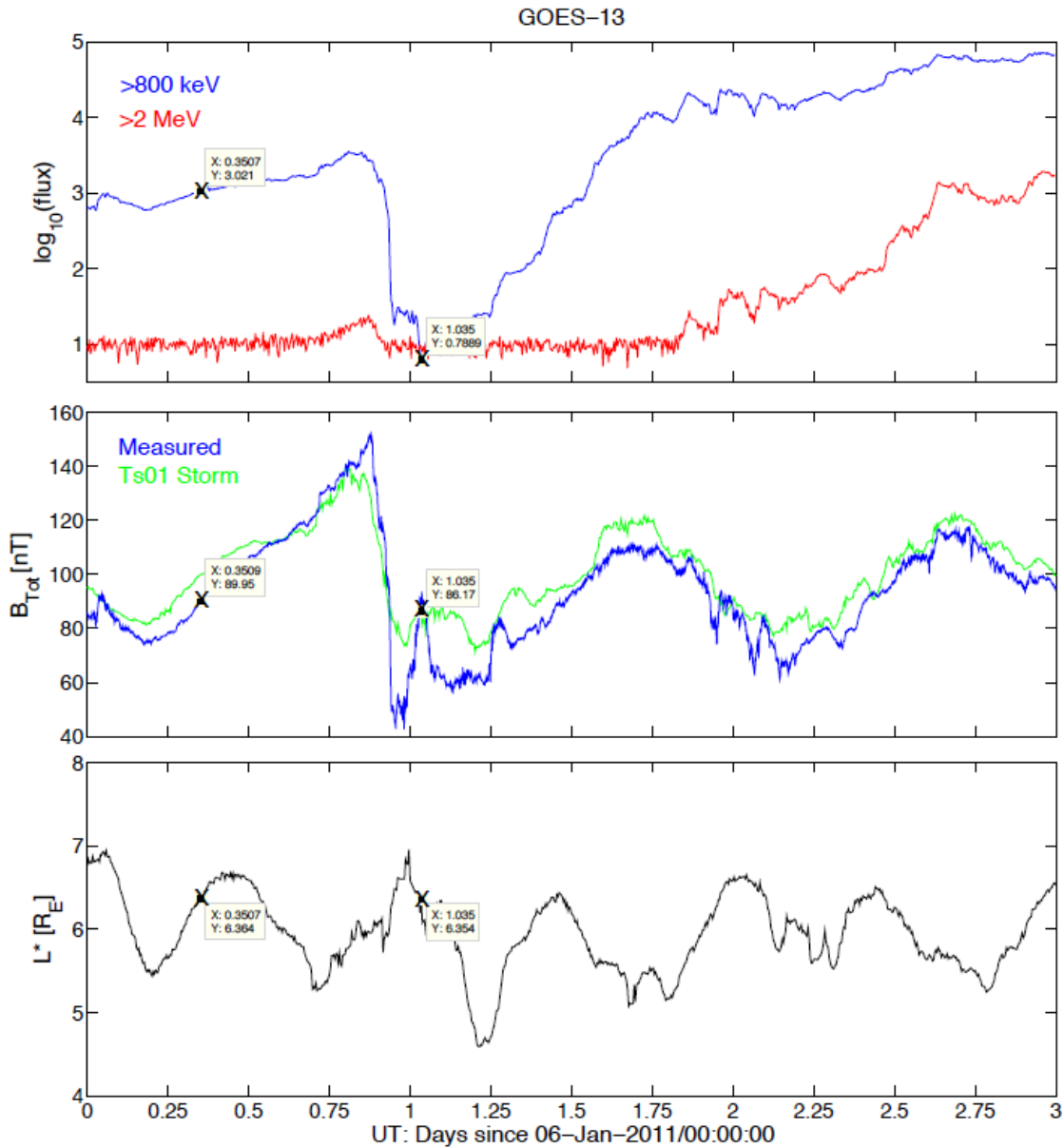
There have been several statistical studies on flux dropouts in the radiation belt. Morley et al. [2010a] presented a flux dropout in response to a solar wind stream interface (i.e. CIR) that occurred on a timescale that they could not explain using conventional diffusion or wave particle interactions. In a follow-up statistical study of 67 events like this [Morley et al., 2010b], they found that the dropouts of  $\sim 0.4$ - $1.8$  orders of magnitude throughout the belt occurred on a timescale of  $\sim 7$  hours. They concluded that conventional diffusion cannot account for the drop at L-shells below  $\sim 6 R_E$ . However, we have shown in this work that when the outer drift shells are depleted suddenly by an inward/outward motion of the magnetopause in response to the pressure pulse in the solar wind, outward radial diffusion acts rapidly (i.e., in only a few

hours) throughout the belt above  $L \sim 4$  resulting in a drop in PSD and an even more drastic drop in flux. From our simple model here and the more advanced modeling of Shprits et al. [2006], the results of Morley et al. [2010a, b] can easily be explained. Concerning this, it is important to note that the inverse of the diffusion coefficient cannot be used to estimate the time scale of the dropouts. The real time scale depends on both the diffusion coefficient *and* the gradient in PSD. The magnetopause shadowing/outward diffusion model explaining sudden flux losses is also consistent with the results of Horne et al. [2009] and Meredith et al. [2011], which were also statistical studies of precipitating electrons during different phases of geomagnetic storms. From over 9 years of data, they found that relativistic electrons experience enhanced precipitation to the atmosphere during the storm-time recovery phase, *not* during the main phase. This is consistent with the results we present here; they reveal that 1) non-adiabatic losses during storm main phase are not primarily to the atmosphere and 2) scattering by wave-particle interactions is most significant during storm recovery phase.

### Additional References Cited in Supplementary Material

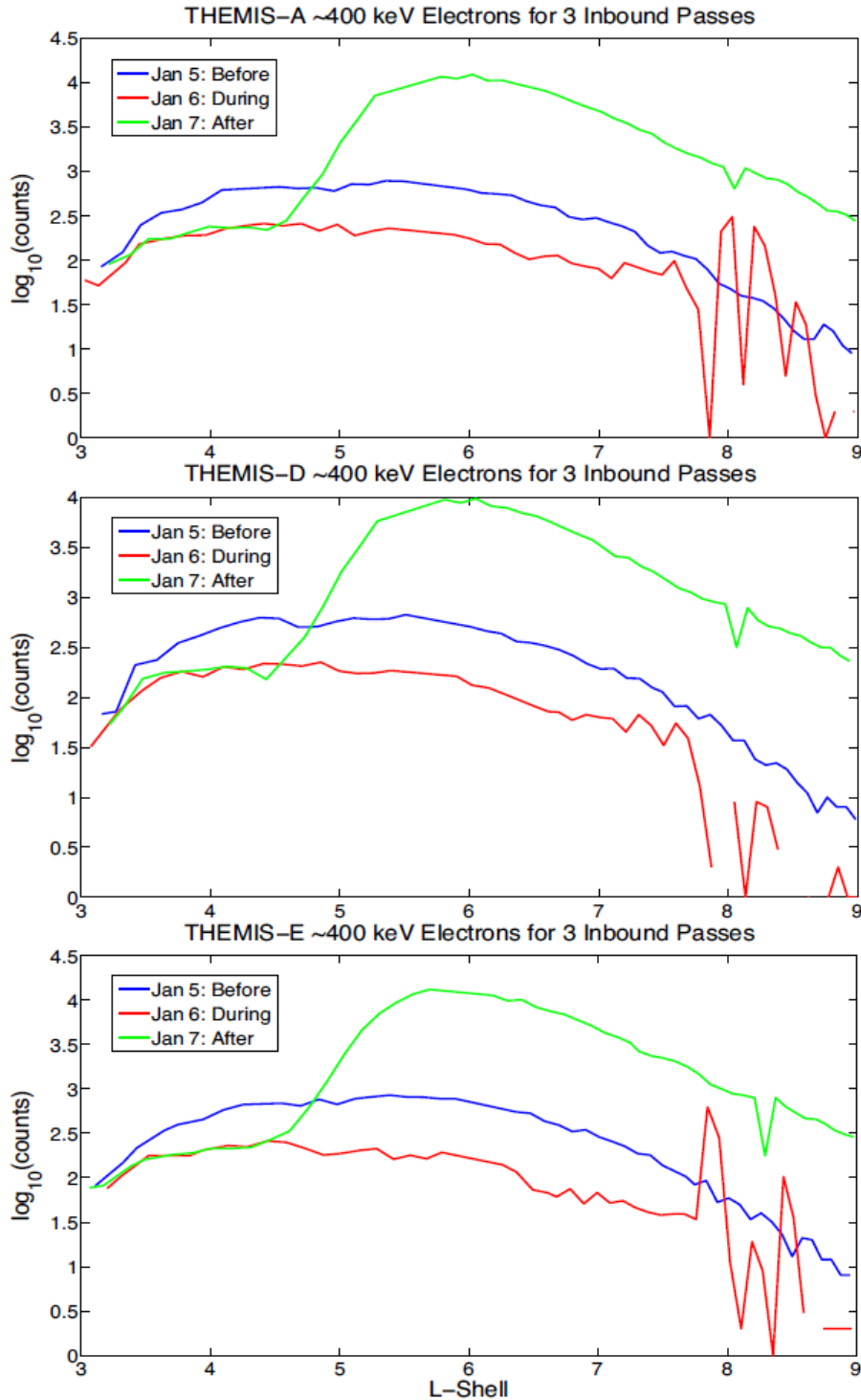
- 1) V. Angelopoulos, The THEMIS Mission, *Space Sci. Rev.*, (2008).
- 2) D. H. Brautigam and J. M. Albert, Radial diffusion analysis of outer radiation belt electrons during the October 9, 1990, magnetic storm, *J. Geophys. Res.*, **105**, 291 (2000).
- 3) D. S. Evans and M. S. Greer, Polar Operational Environment Satellite Space Environment Monitor-2: Instrument descriptions and archive data documentation, *NOAA Tech. Mem.*, **93**, 47, version 1.4 (2004).
- 4) C.-G. Falthammar, Effects of time-dependent electric fields on geomagnetically trapped radiation, *J. Geophys. Res.*, **70**, 2503 (1965).
- 5) J. F. Fennell and J. L. Roeder, Storm time phase space density radial profiles of energetic electrons for small and large K values: SCATHA results, *J. Atmos. Sol.-Terr. Phys.*, **70**, 1760 (2008).
- 6) N. P Meredith. et al., Energetic electron precipitation during high-speed solar wind stream driven storms, *J. Geophys. Res.*, **116**, A05223 (2011).
- 7) Y. Miyoshi et al., Rebuilding process of the outer radiation belt during the 3 November 1993 magnetic storm: NOAA and Exos-D observations, *J. Geophys. Res.*, **108**, 1004 (2003).
- 8) S. K. Morley et al., A rapid, global and prolonged electron radiation belt dropout observed with the Global Positioning System constellation, *Geophys. Res. Lett.*, **37**, L06102 (2010a).
- 9) S. K. Morley et al., Dropouts of the outer electron radiation belt in response to solar wind stream interfaces: global positioning system observations, *Proc. R. Soc. A*, doi:10.1098/rspa.2010.0078 (2010b).
- 10) B. Ni et al., Analysis of radiation belt energetic electron phase space density using THEMIS-SST measurements: Cross-satellite calibration and a case study, *J. Geophys. Res.*, **116**, A03208 (2011).
- 11) C. J. Rodger et al., Use of POES SEM-2 observations to examine radiation belt dynamics and energetic electron precipitation into the atmosphere, *J. Geophys. Res.*, **115**, A04202 (2010).
- 12) R. S. Selesnick and J. B. Blake, On the source location of radiation belt relativistic electrons, *J. Geophys. Res.*, **105**, 2607 (2000).
- 13) N. A. Tsyganenko, A magnetospheric magnetic field model with a warped tail current sheet, *Planet. Space Sci.*, **37**, 5 (1989).
- 14) N. A. Tsyganenko, H. J. Singer, and J. C. Kasper, Storm-time distortion of the inner magnetosphere: How severe can it get?, *J. Geophys. Res.*, **108**, 1209 (2003).
- 15) N. A. Tsyganenko and M. I. Sitnov, Modeling the dynamics of the inner magnetosphere during strong geomagnetic storms, *J. Geophys. Res.*, **110**, A3 (2005).

Fig. S1.



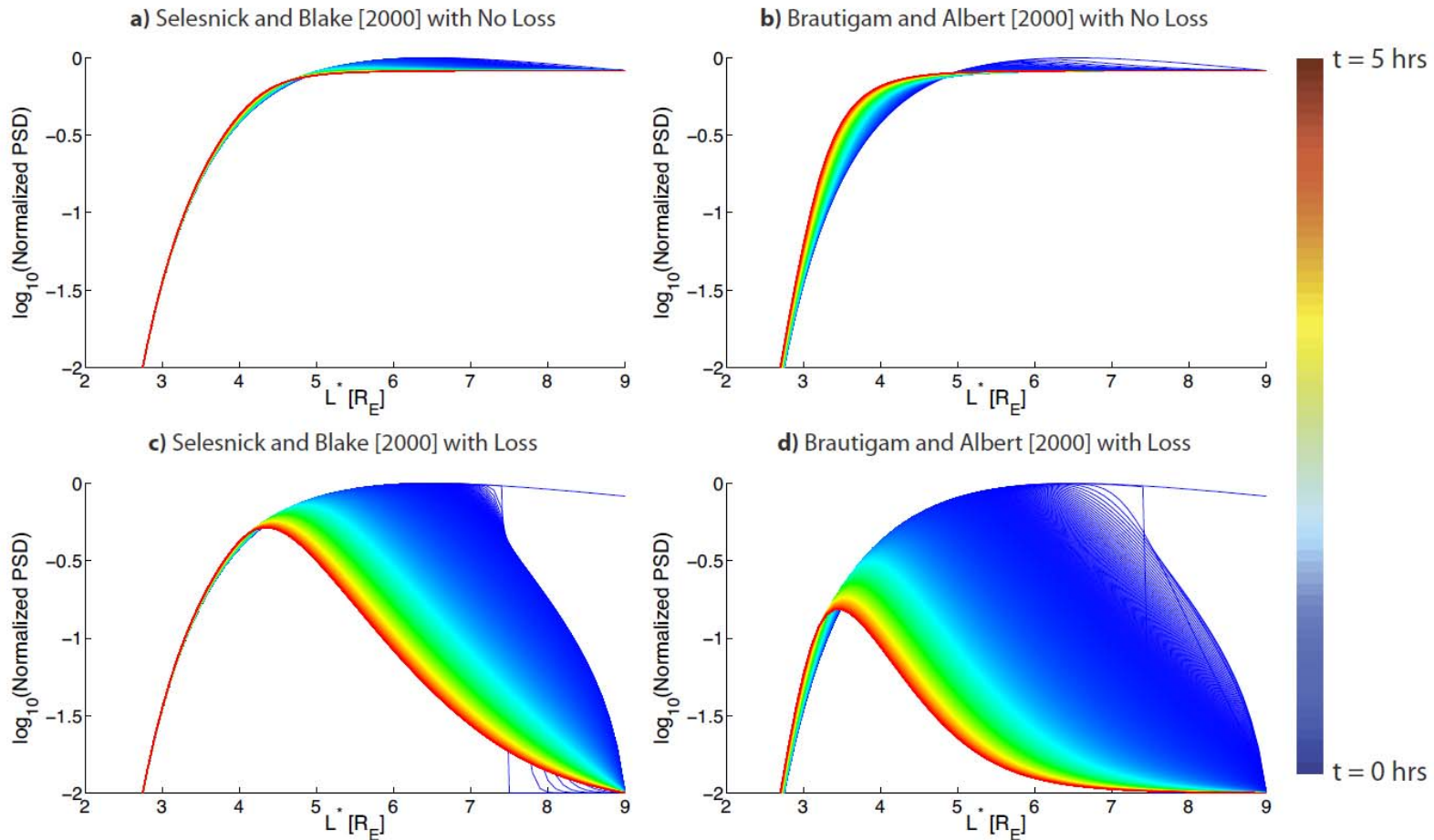
**Figure S1:** Top: GOES-13 flux observations from the  $>800 \text{ keV}$  (blue) and  $>2 \text{ MeV}$  channels. Middle: GOES measured magnetic field (blue) and the Tsyanenko 2001-storm model field at GOES-13 location. Bottom:  $L^*$  calculated for GOES-13 location using the same field model. X's mark the data points, with corresponding X and Y values shown. This clearly shows that the loss of the  $>800 \text{ keV}$  electrons is non-adiabatic. For the two times marked, the  $L^*$  and total field strength are approximately the same, meaning that the electrons' first and third invariants are the same at these times. Assuming that the change is not in pitch angle, which is confirmed with the NOAA observations, then the second invariant is also approximately the same at both times. The flux however, used to calculate the PSD, is two orders of magnitude lower after the dropout, indicating that the PSD for fixed invariants at this time is also significantly lower. Thus, the dropout represents true loss from the system.

Fig. S2



**Figure S2:** THEMIS SST count rates from three inbound passes, before, during, and after the dropout. These count rates, and the TH-A fluxes shown in Figure 2b, are from the first foil-thick coincidence channel, which is not adversely susceptible to contamination like the 12 foil channels. The fluctuations in the counts at higher L-shells during the Jan. 6 inbound pass are a result of the magnetopause flapping over the spacecraft during the high-pressure portion of the CIR.

**Fig. S3**



**Figure S3:** These distributions were generated using a simple 1-D radial diffusion equation with no source and no loss terms. The diffusion coefficients used are those of Selesnick and Blake [2000]:  $DLL = 1e-8 \times Lstar^{10}$  [1/day] for a) and c) and Brautigam and Albert [2000]:  $DLL = 10^{(0.506 \cdot Kp - 9.325)} \times Lstar^{10}$  [1/day] with  $Kp = 5.0$  for b) and d). To simulate loss due to magnetopause shadowing and outward diffusion, the normalized PSD at  $7.5 \leq L^* \leq 10$  RE is dropped to 0.01 shortly after the model starts running (10th time step). This shows that enhanced diffusion can indeed occur in response to a magnetopause-shadowing event and result in a dropout of electrons throughout much of the outer belt in only a few hours (distributions for each time shown in different colors).

**Fig. S4**

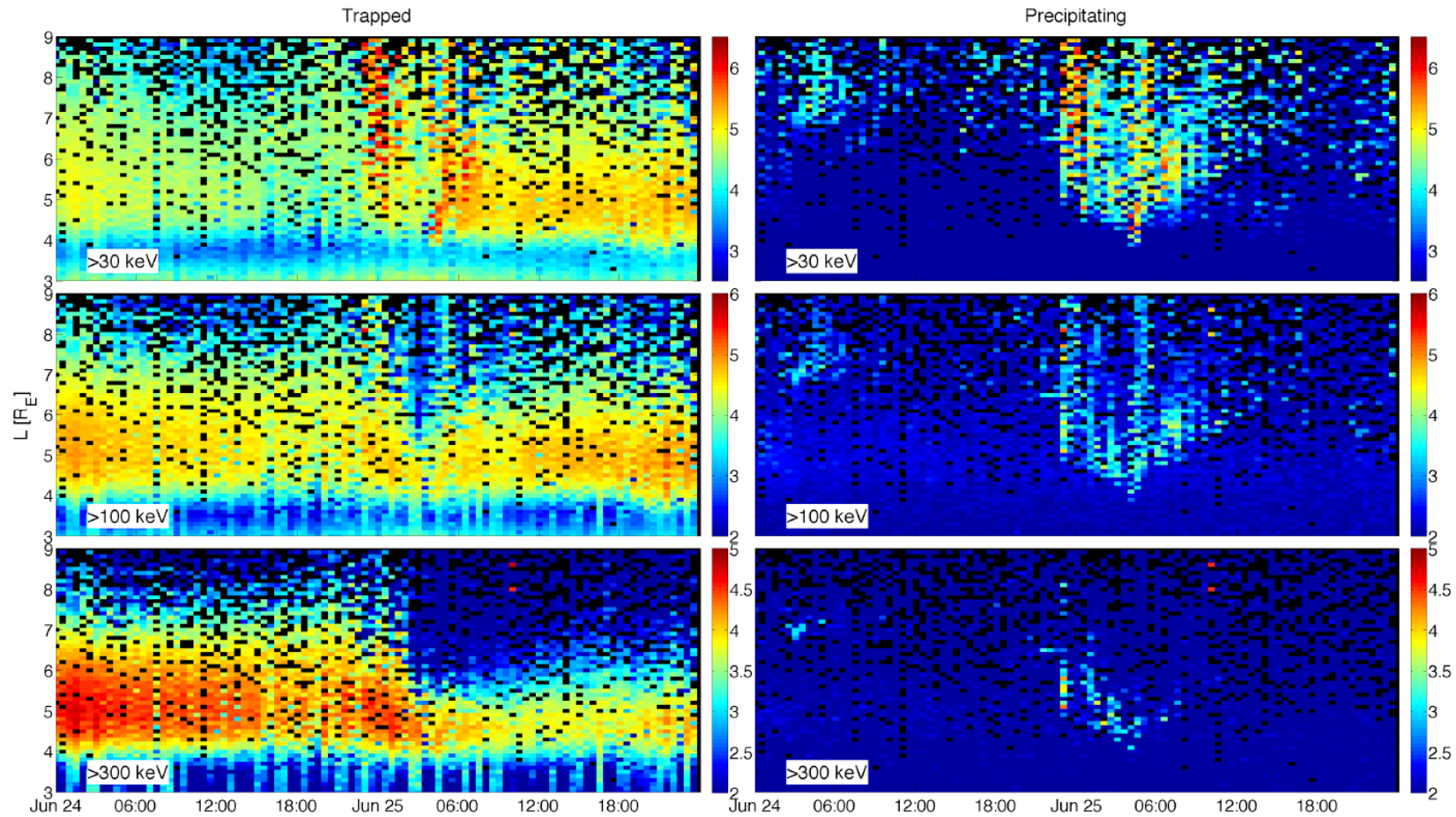


**Figure S4:** NOAA-POES combined data for the 25 June 2008 storm and dropout studied by Loto'aniu et al. [2010]. The minimum magnetopause distance during this event was  $\sim 8.5$  RE. The first significant precipitation event occurs just before 25 Jun at 00:00. This is before the dropout begins. The loss during this event was determined to be non-adiabatic, and the precipitation during the dropout is insufficient to account for the losses and is primarily at L-shells below 5 RE.

**Fig. S5**

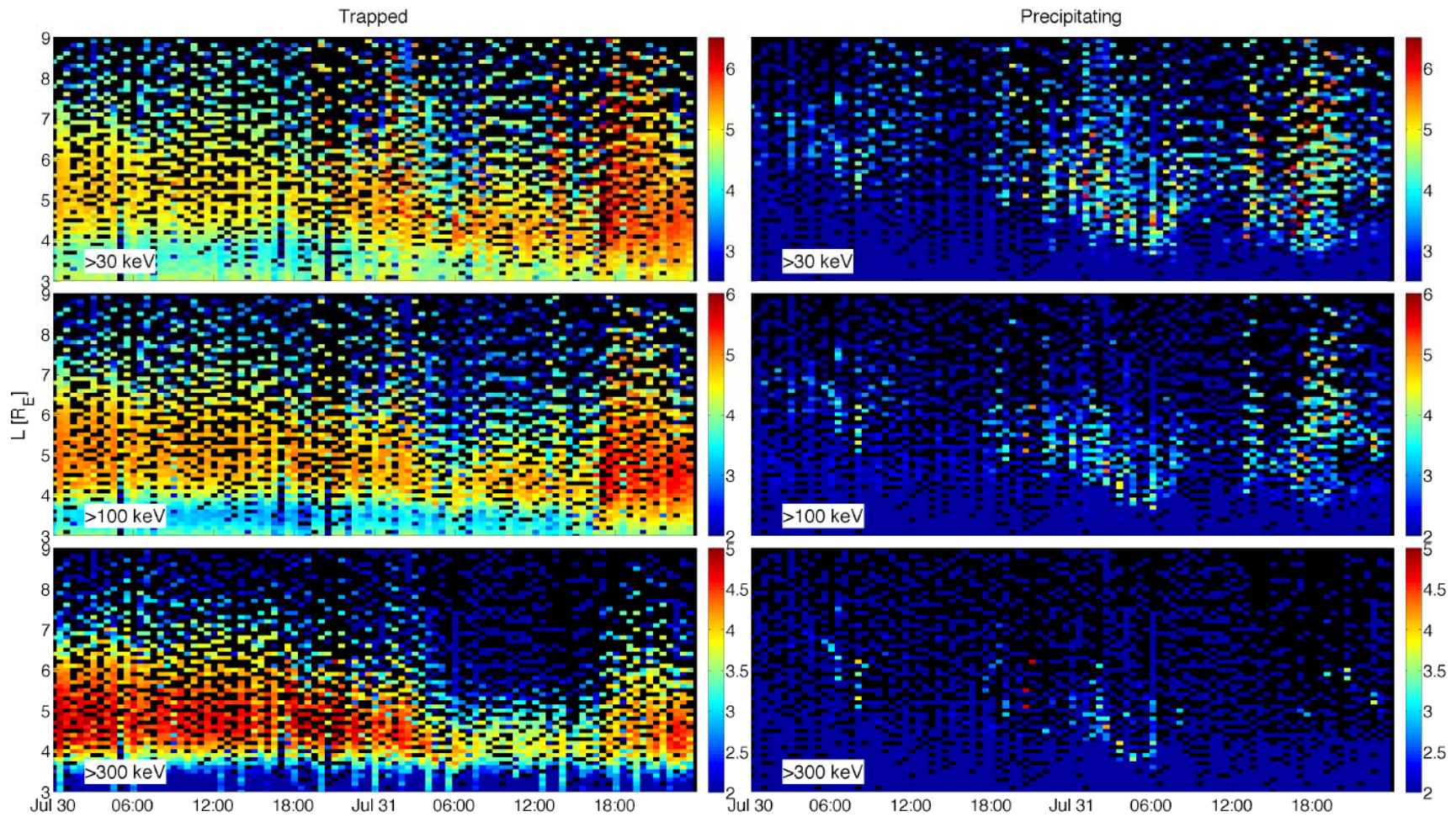


**Figure S5:** NOAA-POES combined data for the 31 July 2001 storm and dropout studied in Green et al. [2004]. The precipitation during the dropout is insufficient to account for the losses and is primarily at L-shells below 5 RE.

**Fig. S6**

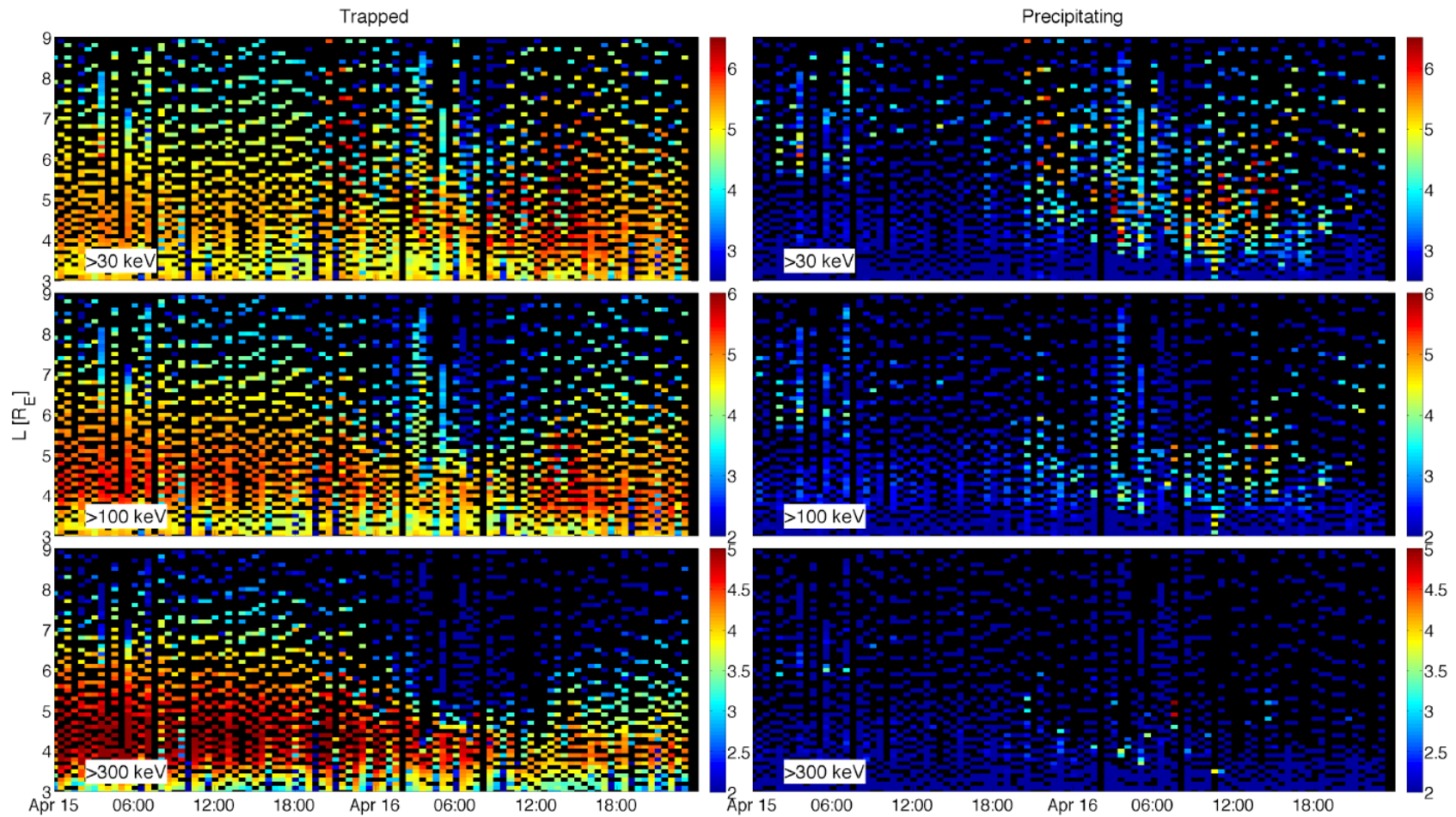


**Figure S6:** NOAA-POES combined data from the 16 April 2000 storm and dropout studied by Onsager et al. [2002]. The loss during this event was determined to be non-adiabatic, and the precipitation during the dropout is insufficient to account for the losses and is primarily at L-shells below 5 RE.

Fig. S7

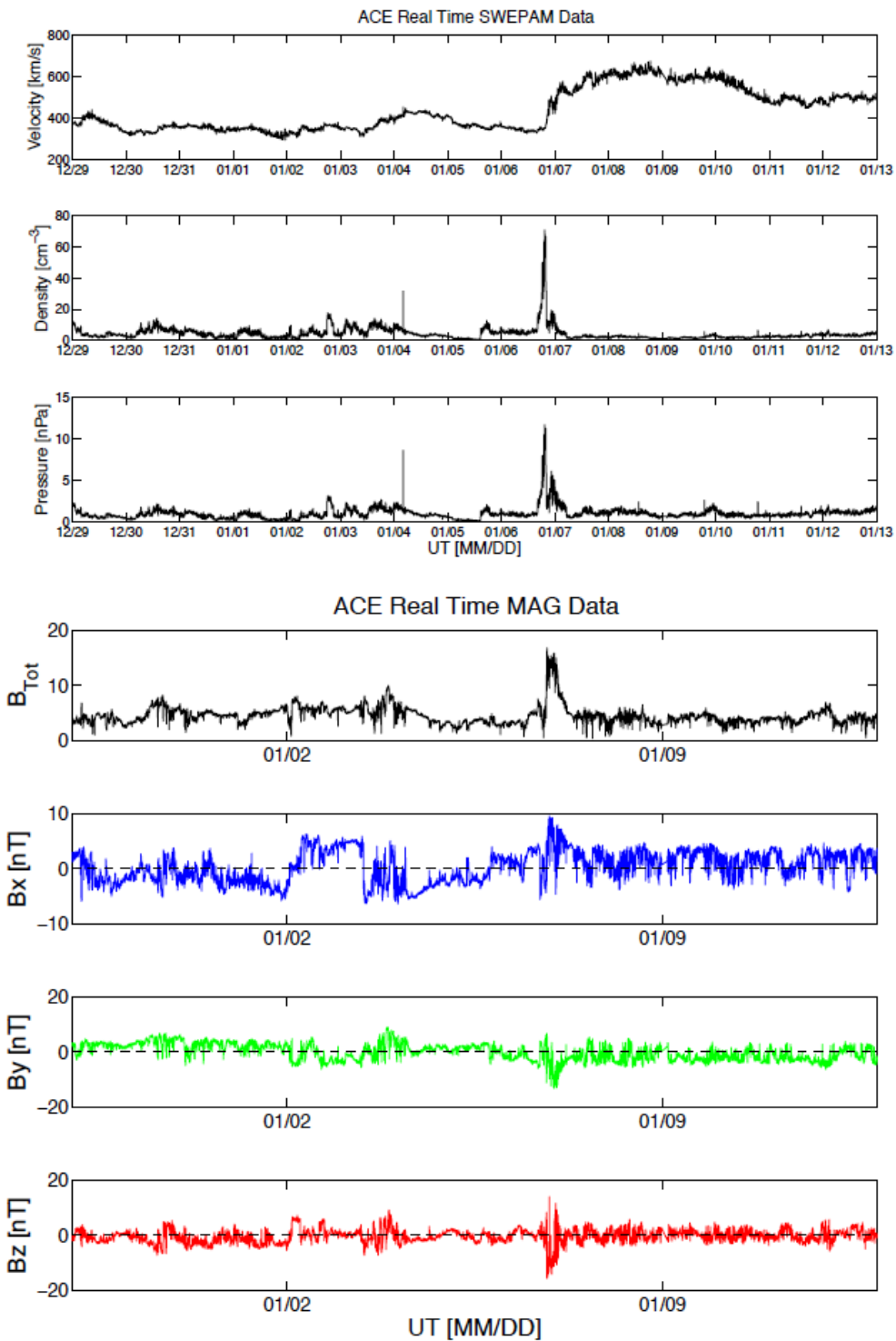
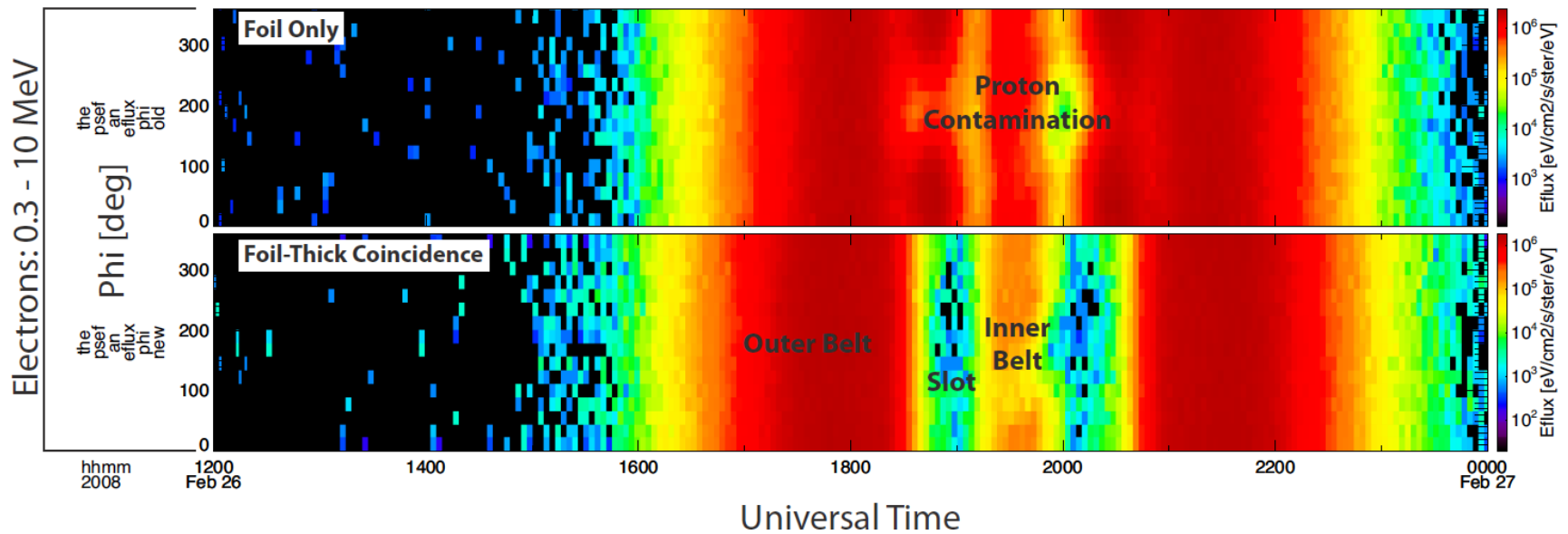


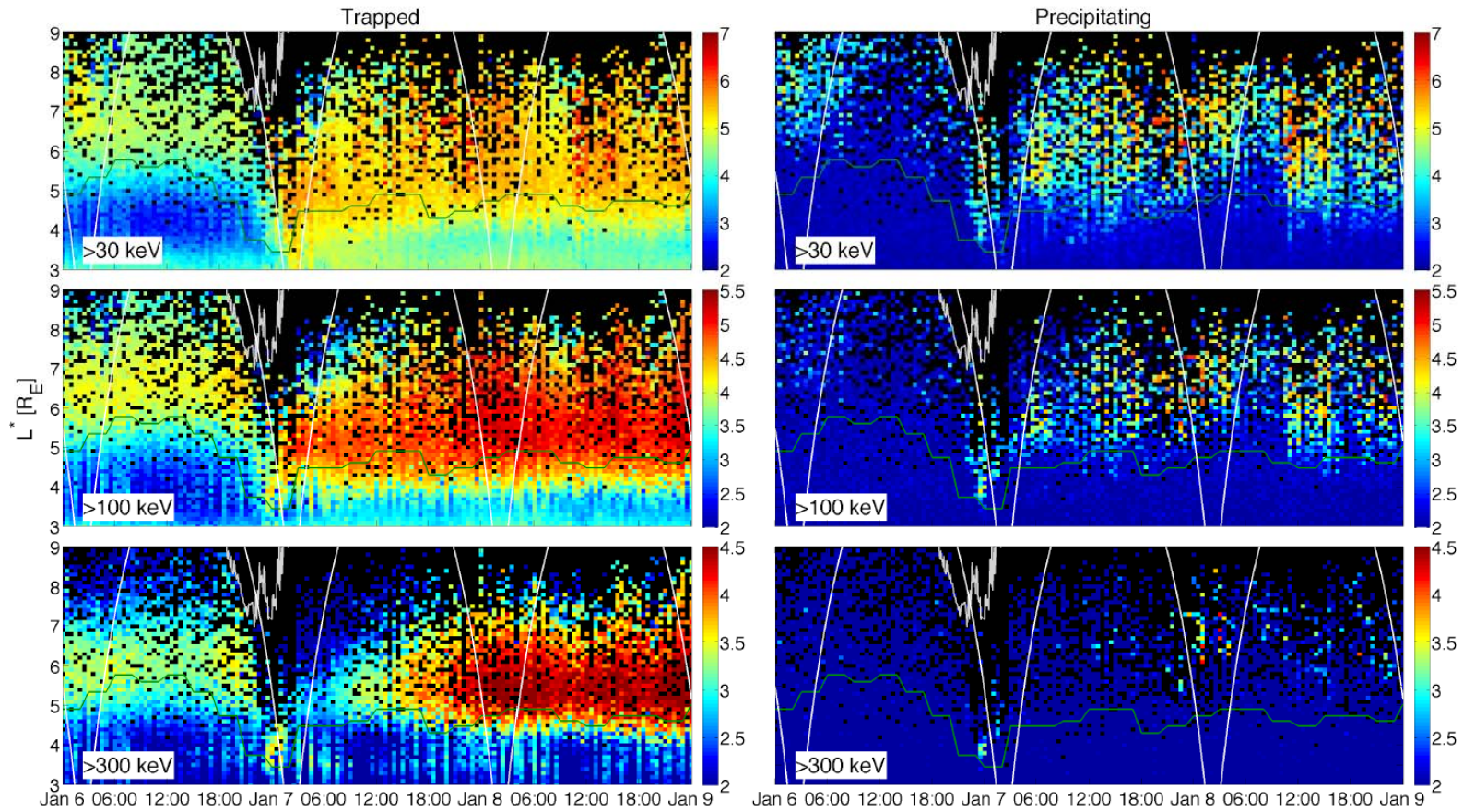
Figure S7: ACE data for 29 Dec. 2010 – 13 Jan. 2011. This confirms the OMNI solar wind data and also shows the conditions both before and after the CIR on 06 Jan 2011.

Fig. S8.



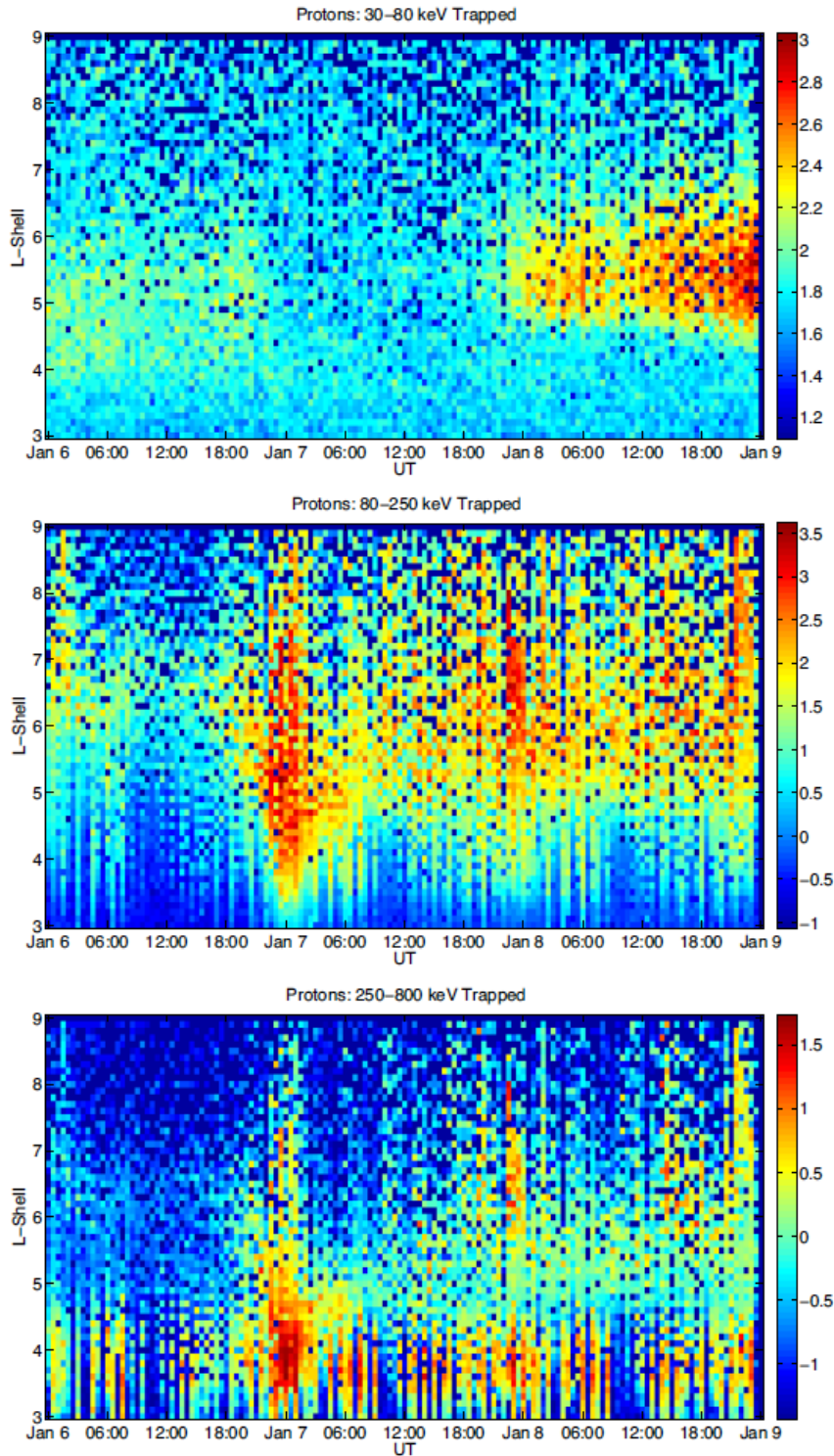
**Figure S8:** THEMIS-E SST spin-plane distributions in energy-flux. The plots show electrons between 0.3 and 10 MeV. The top panel represents data from the “foil” detector for electrons, the detector on the side where a foil prohibits low energy protons from hitting the detector. The bottom plot, however, uses data from the coincidence logic electron channels of the SST that include information from the middle (i.e. “thick”) detector, which cannot be reached by protons less than 6 MeV. The foil-thick channel data thus suppress proton contamination that is known to affect the foil detector and clearly show the presence of the two belts and the slot region. Foil-thick channel data were used in the construction of Figure 2b and Figure S2.

**Fig. S9**



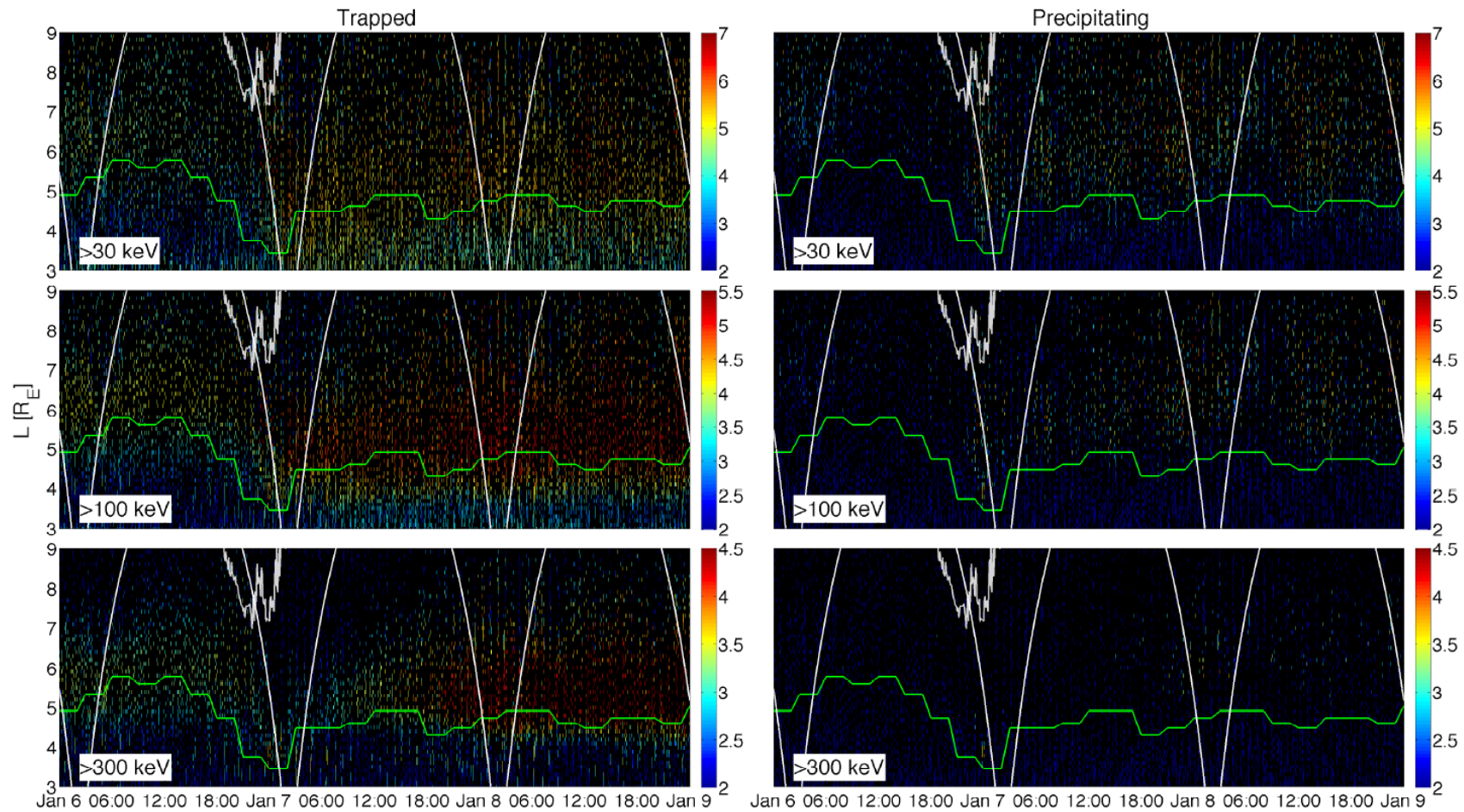
**Figure S9:** NOAA-POES fluxes in the same format as Figure 2a, but instead binned by  $L^*$  calculated using the Tsyganenko-89 magnetic field model. This further supports that the dropout is non-adiabatic.

**Fig. S10**



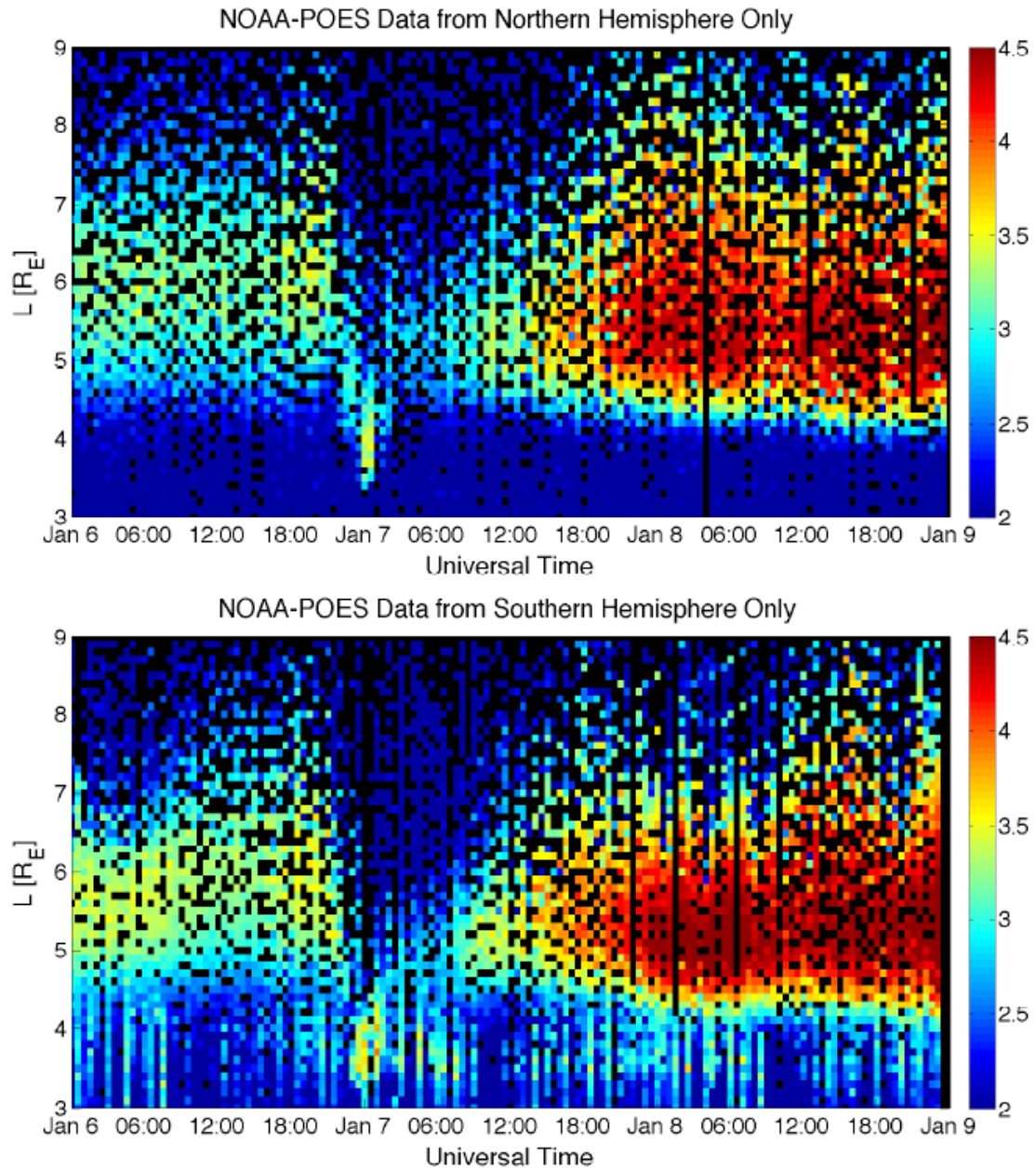
**Figure S10:** Proton fluxes from the NOAA-POES spacecraft. Note that the 30-80 keV protons, which are apparently unaffected by substorm injections, experience a dropout similar to that of the relativistic electrons. The timing for the population to return, however, is notably different from that of the electrons. This supports the concept of loss to the magnetopause via shadowing and outward radial transport.

Fig. S11



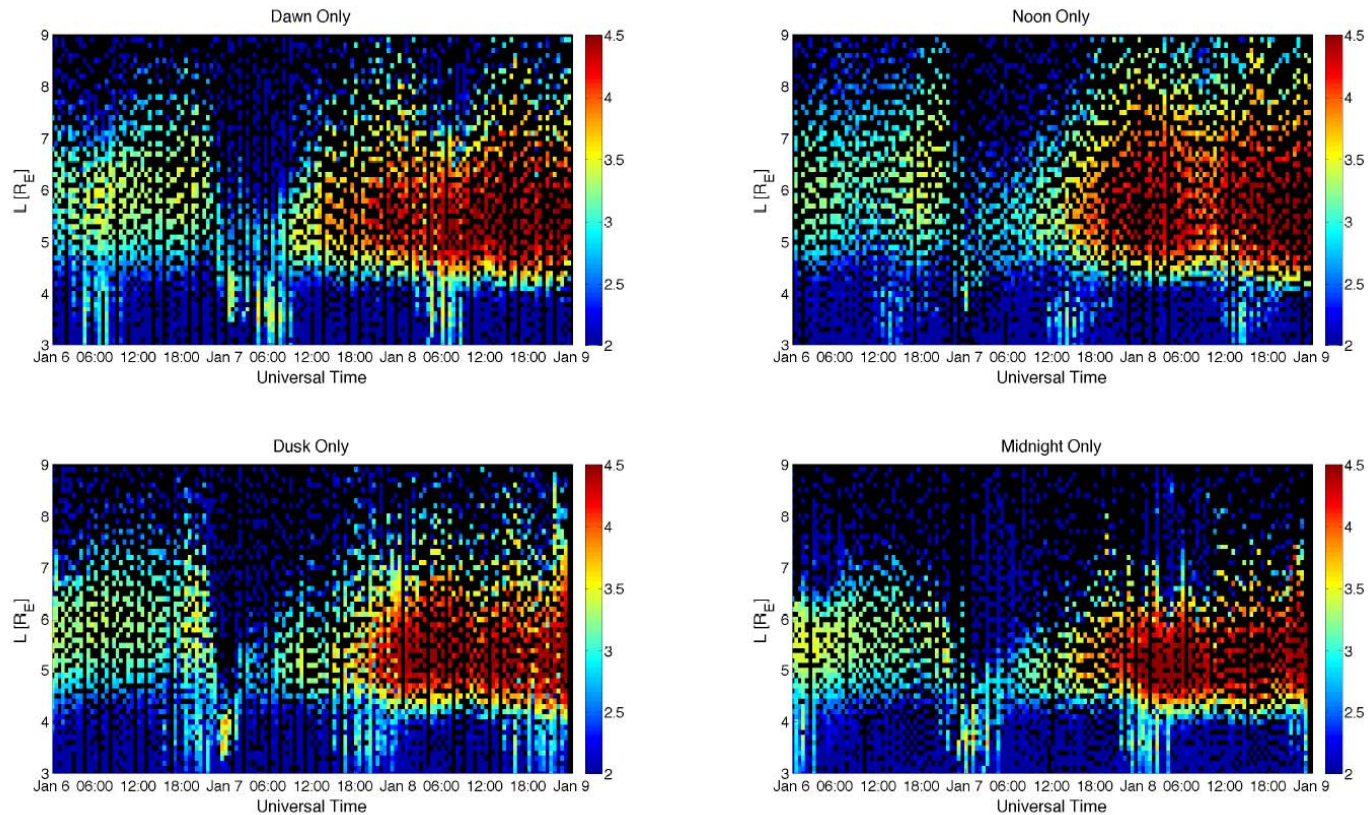
**Figure S11:** NOAA-POES combined MEPED fluxes from all 6 spacecraft at high time resolution (1 minute). This demonstrates that more localized losses in either L or t were not averaged over for the 30-minute resolution plots. Note that with this resolution, the data clearly show insufficient loss to the atmosphere to account for the losses during the dropout.

Fig. S12



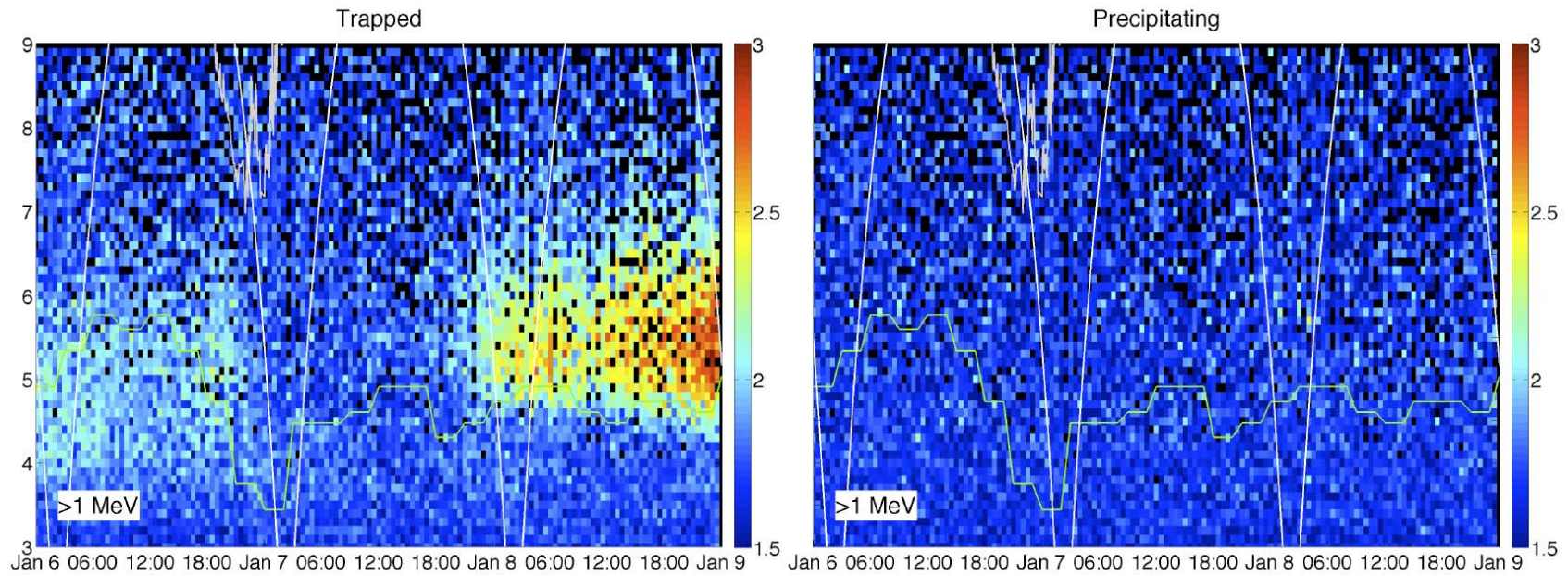
**Figure S12:** NOAA-POES trapped flux data for electrons  $>300$  keV sorted by geographic latitude to show measurements from the Northern and Southern hemispheres. Note that the flux enhancement at  $L \sim 4$  is present in both hemispheres after the dropout occurs at higher  $L$ . This implies that it is a true flux enhancement and not a result of the South Atlantic Anomaly (SAA). Note too the enhanced flux bands at  $L < \sim 4.5$  apparent in the Southern hemisphere data only. These are likely a result of individual spacecraft making observations through the SAA region.

**Fig. S13**



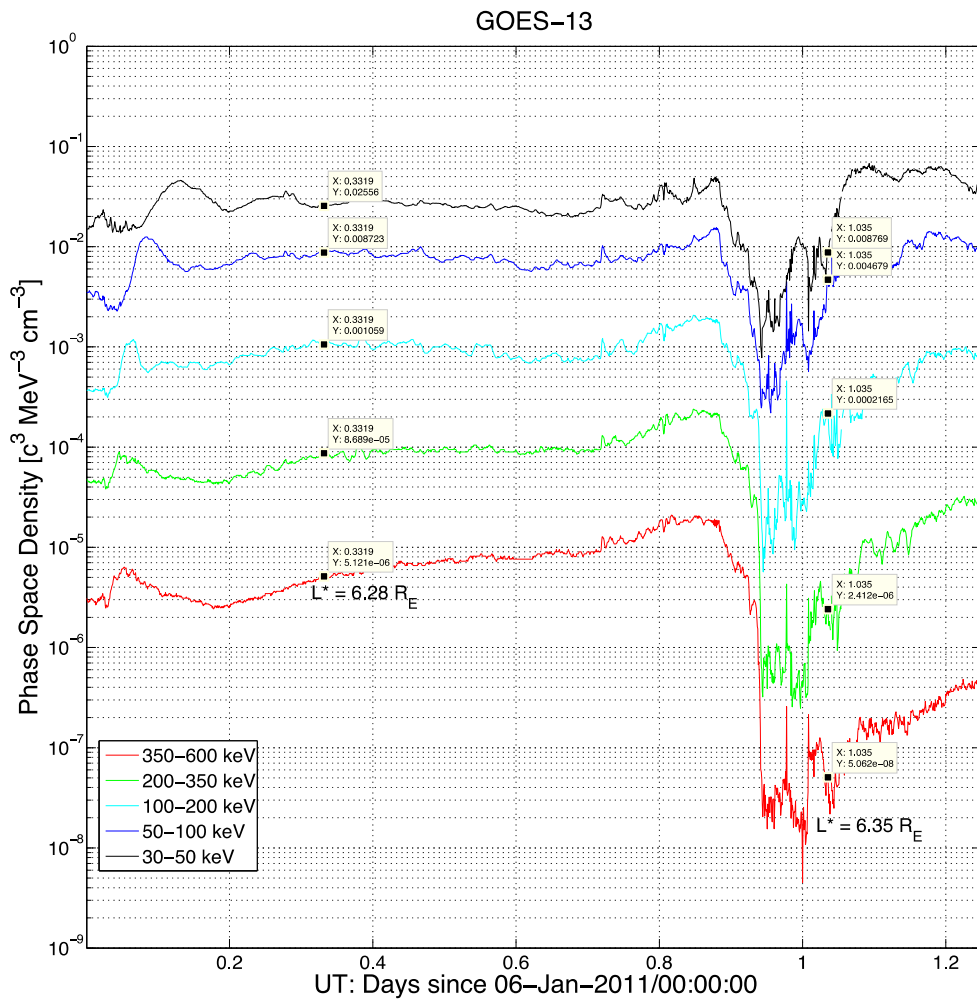
**Figure S13:** NOAA-POES trapped flux data for electrons  $>300$  keV binned by MLT quadrant (Dawn, Noon, Dusk, and Midnight). The South Atlantic Anomaly (SAA) region is clearly seen here in the different local time sectors as the Earth rotates throughout each day. Each day, the SAA is in the midnight quadrant shortly after midnight UT, and it progresses into the dawn, noon, and dusk quadrants around 06:00, 12:00, and 18:00 UT respectively. Note that the flux enhancement at  $L \sim 4$  around 00:00 on Jan 7th is present simultaneously in multiple MLT quadrants, which further shows that it is not a result of the SAA. Also, the dropout occurs about 30 minutes earlier at dusk than at dawn, which supports the idea that the loss is to the magnetopause.

**Fig. S14**



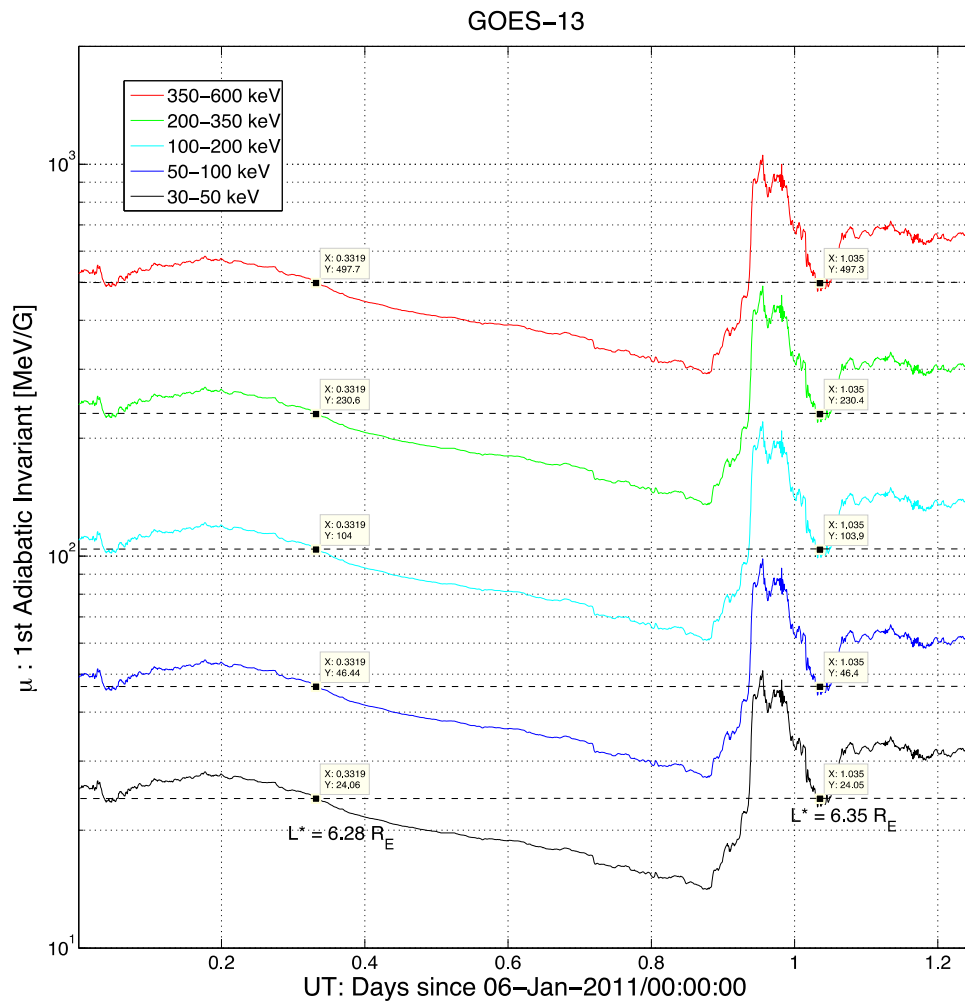
**Figure S14:** NOAA-POES  $>6900$  keV proton fluxes binned by L (0.1 RE resolution) and time (30 min resolution). In the same manner as the previous plots shown, the X-axis is universal time, while the Y-axis is L-shell in units of Earth radii. The color bar shows  $\log(\text{flux})$ . This channel responds primarily to  $>1$  MeV electrons in the outer radiation belt. This confirms that the weak population of  $>1$  MeV electrons before the storm is subject to the same flux dropout experienced by the  $>300$  keV electrons and that an insufficient amount of loss is to the atmosphere during the dropout.

Fig. S15



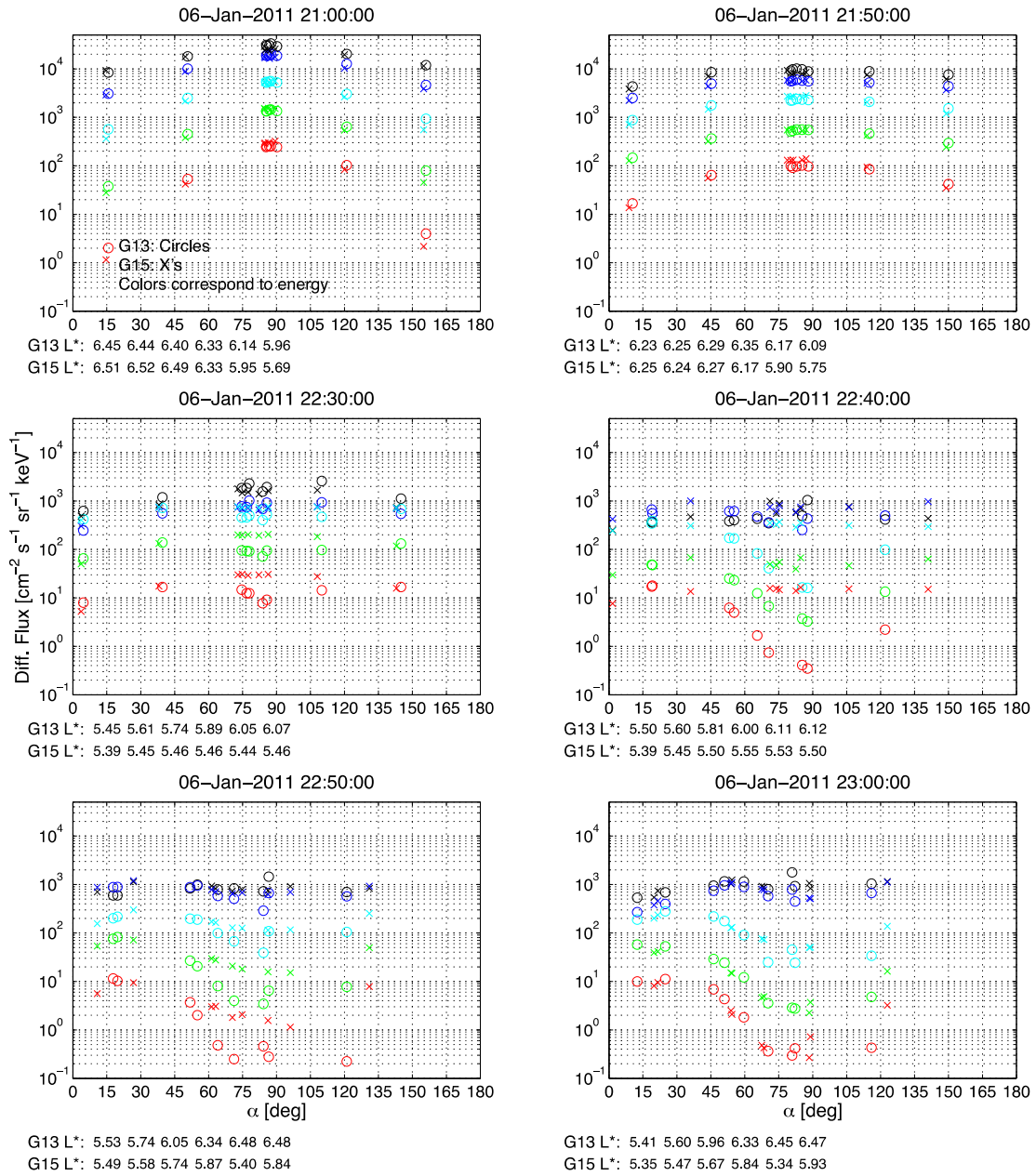
**Figure S15:** Electron phase space densities calculated using GOES-13 differential flux data (colors correspond to energies as listed in the plot legend) for  $\sim 90$  degree pitch angles. Data points marked correspond to times when all three invariants are the same (see also Figs. S16 and S1). For convenience,  $L^*$ s for each marked time are indicated here as well.

Fig. S16



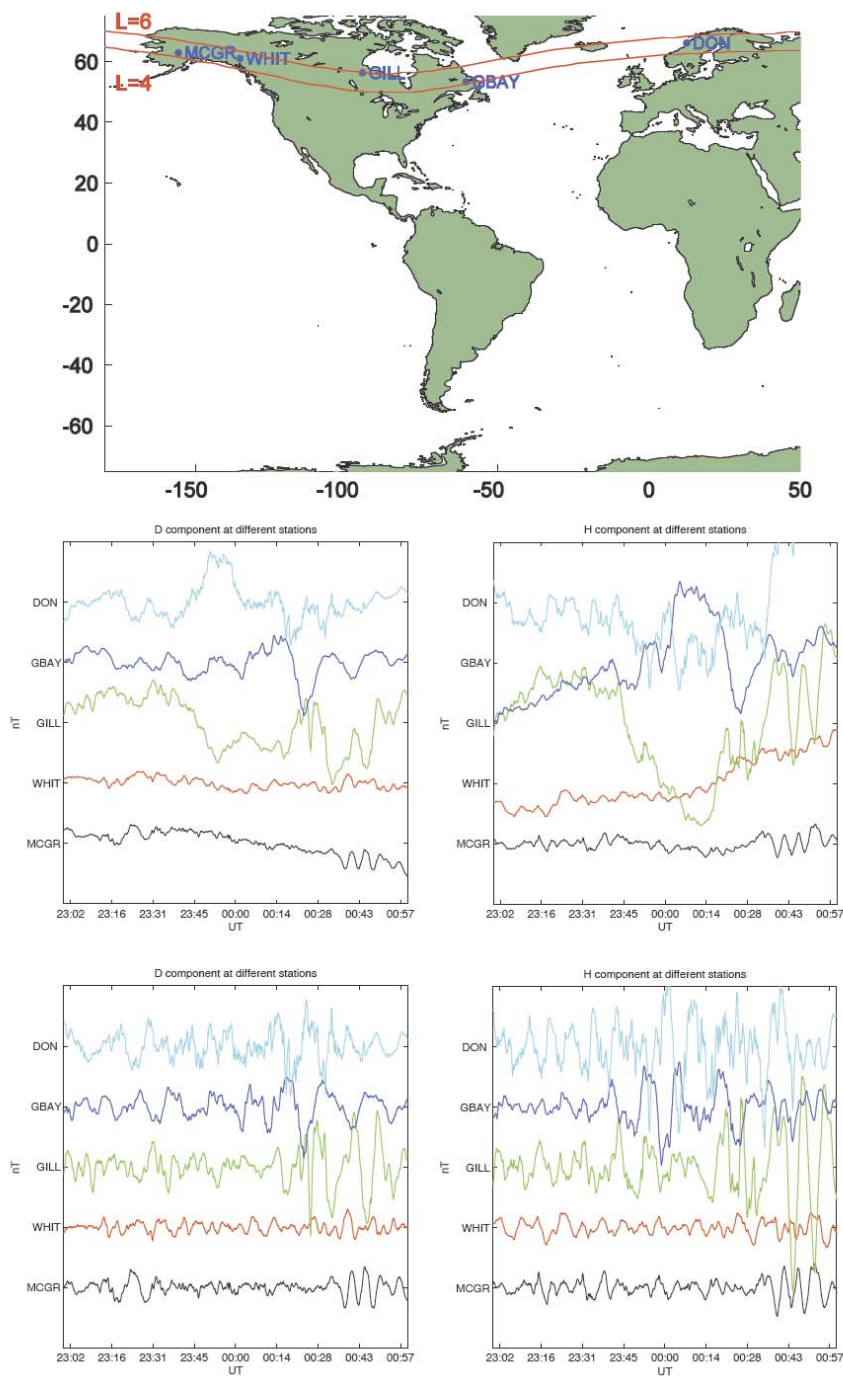
**Figure S16:** Electrons' first adiabatic invariants calculated using GOES-13 differential flux data (colors correspond to energies as listed in the plot legend) and observed magnetic fields for  $\sim 90$  degree pitch angles. Data points marked correspond to times when all three invariants are the same (see also Figs. S15 and S1). For convenience,  $L^*$ s for each marked time are indicated here as well, and horizontal dashed lines serve as reference lines.

**Fig. S17**



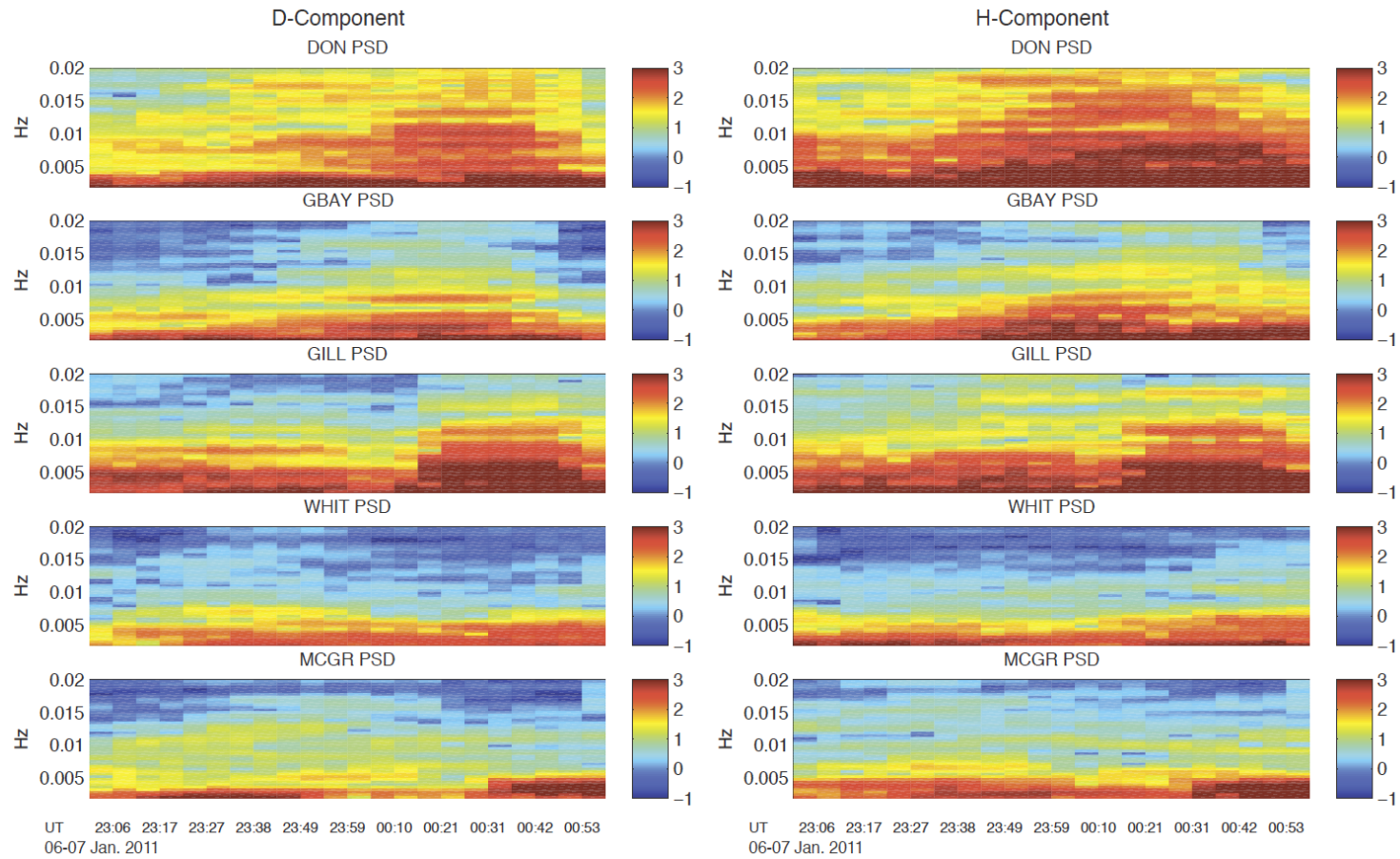
**Figure S17:** Electron flux pitch angle distributions as observed by GOES-13 (circles) and GOES-15 (x's). The six plots show six different times throughout the storm onset and main phases. Different colors correspond to the different energy channels for the MAGED instruments (see corresponding colors in legends of Figures S15 and S16 for corresponding energies). Fluxes are plotted vs. pitch angle, but below each plot, the L's calculated using the Tsyganenko-2001 storm model are also listed.

Fig. S18



**Figure S18:** Magnetometer data from an array of ground stations as shown on the map at top (geographic latitude and longitude shown with L-shells mapped on in red). Unfiltered data is shown in middle row of plots, while filtered data is shown in the bottom row. Distance between tick marks on the vertical axes of the field plots represents 100 nT for the unfiltered data and 50 nT for the filtered data.

**Fig. S19**



**Figure S19:** ULF wave power spectral densities for ground stations shown in Figure S18.

Fig. S20

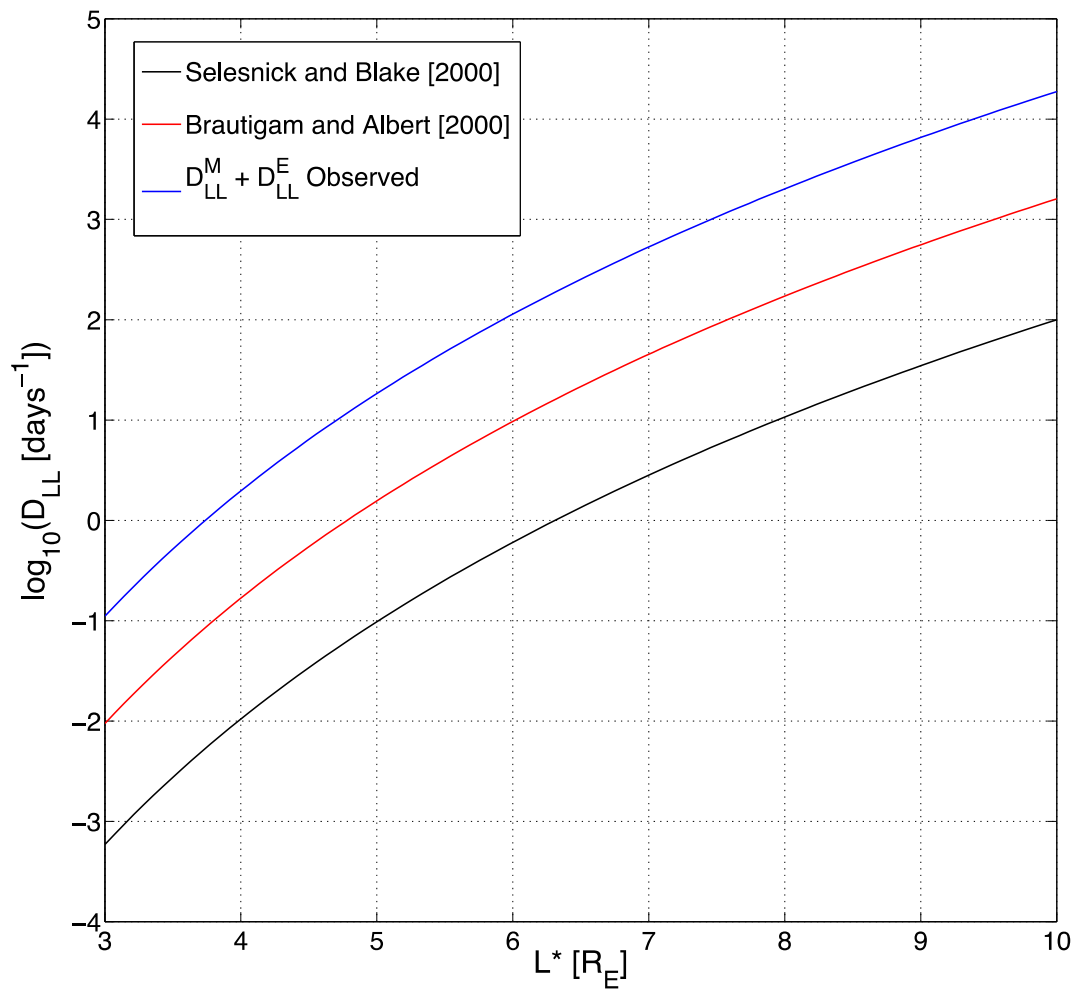


Figure S20: Radial diffusion coefficients calculated from the observed fields during the 06 Jan 2011 event and from the Selesnick and Blake [2000] and Brautigam and Albert [2000] ( $K_p = 5$ ) models.